Icarus 387 (2022) 115183

Contents lists available at ScienceDirect

Icarus

journal homepage: www.elsevier.com/locate/icarus

Research Paper

# Cellular patterns and dry convection in textured dust storms at the edge of Mars North Polar Cap

A. Sánchez-Lavega [a,*], A. Erkoreka [b], J. Hernández-Bernal [a,b], T. del Río-Gaztelurrutia [a], J. García-Morales [b], I. Ordoñez-Etxeberría [c], A. Cardesín-Moinelo [d], D. Titov [e], S. Wood [f], D. Tirsch [g], E. Hauber [g], K.-D. Matz [g]

[a] Universidad del País Vasco, Bilbao, Spain
[b] Aula EspaZio Gela, UPV/EHU, Bilbao, Spain
[c] Planetario Pamplona, Spain
[d] European Space Agency, ESAC, Madrid, Spain
[e] European Space Agency, ESTEC, Noordwijk, Netherlands
[f] European Space Agency, ESOC, Darmstadt, Germany
[g] German Aeroespace Center (DLR), Institute of Planetary Research, Berlin, Germany

ARTICLE INFO

*Keywords:*
Mars
Atmospheric dynamics
Dust storms
Cellular Convection

ABSTRACT

We present a study of textured local dust storms that develop at the northern polar cap boundary on Mars springtime. We have used images obtained with VMC and HRSC cameras onboard Mars Express and MARCI on MRO to analyze dust storms captured from March to July 2019 (Ls = 350° in MY 34–Ls = 54° in MY 35). The textured storms grow in the longitude sector 150°E-210°E centered at latitude ~60°N and exhibit spiral, filamentary and compact shapes that change and evolve rapidly in a daily basis. The storms translate by prevailing east and southeast winds with speeds 15–45 $ms^{-1}$. In some areas of their interiors they show organized clusters of cells formed typically by 100 elements with sizes ~5–30 km with a length/width ratio ~ 1.2–3 in the wind direction. The cells have elongated downwind tails with lengths 4–8 times the cell size. The cells top altitudes are ~6–11 km above their surroundings. We propose that the spirals grow as baroclinic vortices within a vertically sheared eastward jet present at this epoch in Mars due to the intense meridional temperature gradient at the polar cap edge. We show using a simple one-dimensional model that the cells can be produced by shallow dry convection with dust acting as the heating source to generate the updrafts. These patterns resemble those seen in laboratory experiments and on clouds in Earth's atmosphere and can serve to comparatively elucidate and discern the different mechanisms at work in each case.

## 1. Introduction

Springtime season in Mars' northern hemisphere (Ls = 0° - 90°) is characterized by rich atmospheric dynamical activity that takes place at the edge of the polar cap, often revealed by the presence of local dust storms. Disturbances are triggered by the temperature gradient between the receding polar ice layer and the surrounding terrain, enhanced by the orographic properties of the northern hemisphere (James et al., 1999; Cantor et al., 2010; Wang and Ingersoll, 2002; Hinson and Wilson, 2021; Clancy et al., 2017; Khare et al., 2017). These dynamical instabilities show a variety of morphologies in images from orbit spacecraft, variously organized in cyclonic spirals, arc shapes, bands and commas, sometimes accompanied by water ice clouds (Wang and Fisher, 2009; Guzewich et al., 2015).

In this paper we focus in a particular case of textured dust storms characterized by the presence of large areas of organized granular or cellular patterns, mixed with other forms denoted as puffy and pebbled (Kulowski et al., 2017), and ruffled elongated features (Heavens, 2017). Our aim is to characterize the properties of the cellular compact structures and of the storms themselves, and to gain insight on the mechanisms operating behind them. We concentrate in the study of two main textured storm systems evolving at the edge of the North Pole, but we show two additional cases to illustrate the variety of disturbances that can take place under a priori similar atmospheric conditions. These

* Corresponding author.
*E-mail address:* agustin.sanchez@ehu.eus (A. Sánchez-Lavega).

https://doi.org/10.1016/j.icarus.2022.115183
Received 18 April 2022; Received in revised form 20 June 2022; Accepted 11 July 2022
Available online 14 July 2022

storms changed rapidly but were recurrent, forming, destroying and re-forming from sol to sol at the same location.

This study is based on a combined imaging survey from two orbiting spacecraft, Mars Reconnaissance Orbiter (MRO) and Mars Express (MEX) covering the period from 3 March to 17 July 2019 (Ls = 350° in MY 34–Ls = 54° in MY 35). This period corresponds to the early springtime season in the northern hemisphere, before aphelion at Ls = 71°, and about one Earth year after the Global Dust Storm of 2018 (Sánchez-Lavega et al., 2019). The survey covers all longitudes between latitudes 45°N to 90°N. During this period, the edge of the polar cap receded from latitude 57°N to 72°N (del Río-Gaztelurrutia et al., 2021). The combination of images from different orbits (MRO is sun-synchronized and MEX is polar elliptical) allows expansion of the local time coverage.

## 2. Observations

A first group of images were obtained by the Visual Monitoring Camera (VMC, Sánchez-Lavega et al., 2018a) and by the High Resolution Stereo Camera (HRSC, Jaumann et al., 2007; Gwinner et al., 2016), both onboard the Mars Express spacecraft, which is in a polar elliptical orbit (pericenter altitude ~300 km, apocenter altitude ~10,000 km, period ~7.5 h) (Table 1). VMC is a small camera with a FOV of 40° x 31° and it operates with a bayer pattern in the wavelength range 400–650 nm. The maximum spatial resolution of the images used in this study was in the range 6–12 km/px. These images were analyzed using the ELKANO software (Hernández-Bernal et al., 2019). HRSC has four color channels, two stereo channels, two photometry channels and one nadir channel covering the following spectral ranges: BL (blue channel 440 ± 45 nm), GR (green channel 530 ± 45 nm), RE (red channel 750 ± 20 nm) and IR (near infrared channel 970 ± 45 nm). The map-projected scale of the images used here is 0.8 km/px. HRSC images were radiometrically corrected and orthorectified using software developed at DLR and then transferred into ArcGis software (2022). The second group of images were obtained with the Mars Colour Imager MARCI onboard MRO (Bell III et al., 2009; Cantor et al., 2010), a spacecraft in a circular sun-synchronized orbit with altitude ~250 to 316 km and period ~1.86 h. We used images from MARCI optical channel with a wavelength coverage from 437 to 718 nm with a resolution of 1 km/px. These images were analyzed using the software ISIS-USGS (2022) for processing and map projection and QGIS (2022) for measurements.

**Table 1**
Image identification.

| | Month | Day-UT | LTST |
|---|---|---|---|
| HRSC image | | | |
| 19,461: 2019 | 05 | 22 T08:36:22.458 | 11:20:53 |
| 19,475: 2019 | 05 | 26 T10:16:18.455 | 07:09:10 |
| 19,513: 2019 | 06 | 06 T11:22:49.422 | 22:52:39 |
| 19,527: 2019 | 06 | 10 T13:16:17.471 | 16:28:51 |
| | | | |
| MARCI Year | | | |
| 2019 | 05 | 22–09:09 | 13:27 |
| 2019 | 05 | 23–09:28 | 13:07 |
| 2019 | 05 | 24–09:46 | 13:07 |
| 2019 | 05 | 25–11:57 | 13:36 |
| 2019 | 05 | 26–02:55 | 13:31 |
| 2019 | 05 | 26–10:24 | 13:27 |
| 2019 | 05 | 27–01:21 | 13:04 |
| 2019 | 05 | 27–23:48 | 13:12 |
| 2019 | 05 | 28–12:53 | 14:17 |
| 2019 | 05 | 29–13:12 | 13:17 |
| 2019 | 05 | 29–15:04 | 15:08 |
| 2019 | 05 | 30–13:31 | 13:17 |
| 2019 | 05 | 31–13:49 | 13:17 |
| | | | |
| VMC_SR image | | | |
| 190525_220013_004 | 05 | 25–22:00 | 07:42 |
| 190527_015607_004 | 05 | 27–01:56 | 13:12 |
| 190529_174527_006 | 05 | 29–17:45 | 16:42 |
| 190529_184931_086 | 05 | 29–18:49 | 17:48 |
| 190603_023343_010 | 06 | 03–02:33 | 08:00 |
| 190604_000241_005 | 06 | 04–00:02 | 17:12 |
| 190604_003129_041 | 06 | 04–00:31 | 17:42 |
| 190705_014207_004 | 07 | 05–01:42 | 12.10 |
| 190709_050358_007 | 07 | 09–05:03 | 11:42 |

Measurements of the latitude and longitude of the positions on the disk of selected targets are used to calculate the size of selected features from their angular separation between two extreme points 1 and 2 in Mars' surface according to

$$L = R_{Mars} cos^{-1}(sin\varphi_1 sin\varphi_2 + cos\varphi_1 cos\varphi_2 cos(\lambda_2 - \lambda_1)), \quad (1)$$

where ($\varphi_1$, $\varphi_2$) and ($\lambda_1$, $\lambda_2$) are the latitudes and longitudes of points 1 and 2 and $R_{Mars}$ is Mars' radius. The positions of targets at different times are used to calculate the zonal ($u$) and meridional ($v$) components of their velocity.

## 3. Disturbance identification

Fig. 1 shows a map of the Northern Hemisphere with the identification and location of the different disturbances tracked during the period covered by our observations, and marks the individual storms that will be analyzed in detail below. We identified disturbances with the following morphologies: (S1) textured dust storms (with cellular or granular patterns), compact or organized in spiral systems; (S2) Irregularly shaped or filamentary and (S3) flushing arc-shaped dust storms. Most storms are accompanied by large areas of hazes and clouds of water ice with a non-defined or irregular morphology. We note that there is a high concentration of activity in the longitude sector from 180°E to 360°E. These dust storms have areas $<1.6 \times 10^6$ km$^2$ and thus they are classified as of local type (Cantor et al., 2001). Textured storms S1 are the main objective of this work, and we essentially focus our study in two selected storms, denoted S1A and S1B in Fig. 1, which evolved at the edge of the North Polar Cap (NPC) in a short period from 22 May to 6 June 2019.

## 4. Textured storm S1A

Storm S1A was tracked from 22 to 29 May 2019 ($L_s$ = 28°–32°). It was centered at latitude 67°N but extended from ~60$^0$N to 75$^0$N (penetrating the North Polar Cap) in the longitude sector 180°E-210°E in Arcadia Planitia (Figs. 2, 3–10). S1A formed, evolved significantly, disappearing and reappeared from sol to sol, showing major morphological changes in a time scale of hours (Fig. 2). The repetitive dissipation and generation with different morphologies indicates that the disturbance is highly sensitive to small changes in sol-to-sol atmospheric conditions at the same or a very close location. Because of its repetitive appearance every 3-4 days, storm S1A could form part of a series of disturbances (a storm cluster) propagating eastward.

The images taken in May 22 showed S1A centered at longitude ~190°E and extending from latitudes ~40°N to 73°N, penetrating on the polar cap (Fig. 3). It was formed by three parallel filaments oriented perpendicularly to the NPC and occupying a total area of ~$4.3 \times 10^5$ km$^2$. The length, width and separation between them are given in Table 2. At a smaller scale, the filaments are formed by a series of elongated and regularly spaced dust masses similar to the ruffled forms described by Heavens (2017), with a width of ~10–20 km and length 20–50 km (Fig. 4a, b). The head of these features are compact dust cells with a size of 7 km, regularly distributed with separations between consecutive head centers of ~25 km (Fig. 4c, d) (Table 3). The morphology suggests that a tail forms behind the head (the cell) when the wind blows the dust in the South-East direction at about 45° south from the parallel circle, generating the elongated features. The pattern also reveals a change in the wind direction and dust morphology

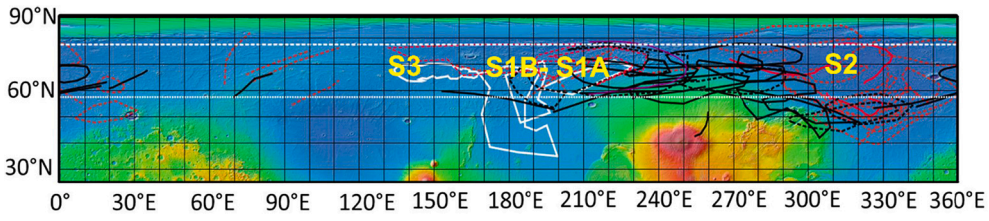


**Fig. 1.** Topographic map of Mars northern hemisphere showing the tracks of dynamical instabilities observed from 3 March to 17 July 2019 (Ls = 350° of MY 34 to 54° of MY 35). Different kinds of features are marked with lines and colors: white for the cellular textured dust storm clusters (S1A-S1B); red for irregular morphology storm clusters (S2) and arc-shaped ("flushing") dust storms (S3); and black for condensate hazes (dashed line) and cloud (continuous line) systems (not dust) without a defined morphology. The edge of the NPC is marked by white lines (dotted for Ls = 0° and dashed for Ls = 88°). The reference map is from JMARS (Java Mission-planning and Analysis for Remote Sensing; https://jmars.asu.edu/) based on data gathered by the Mars Global Surveyor (MGS) spacecraft using the Mars Orbiter Laser Altimeter (MOLA). (For interpretation of the references to colour in this figure legend, the reader is referred to the web version of this article.)

southward of latitude 50°N, when comparing the morphology in filaments 1–2 and filament 3 (Fig. 4a). The regular separation between these elongated features (in particular in the three filaments northward of 50°N) suggests the action of a wave mechanism.

In May 23, there was no storm in MARCI images (Fig. 2). On 24 May a single-band dust storm appeared, elongated in the north-south direction, centered at 198°E and extending between latitudes 45°N and 65°N (Fig. 5a). Because of these properties, we identify it as re-formed dust storm S1A. In May 25, the storm had expanded equatorward, forming a large band (from latitudes 38°N to 73°N) centered at 180°E longitude (Fig. 5b). The cellular pattern is more irregular in shape, but still prominent, with compact cells of ~10–15 km, as heads of elongated features (Fig. 5c, d), projecting their shadows on the background.

These observations show the cyclic, recurrent behavior (from sol to sol) of a dust storm which forms and disappears at the same local time and in close locations, but with variable morphology and extent (Fig. 2). From 22 to 25 May, the changes in S1A extension and morphology are significant, although when present, the storm preserves its main structure (north-south band-shape and presence of cellular or granular patterns). The observations show that although the atmospheric conditions in the area do not change significantly from one sol to another, small differences are enough to trigger or not to trigger the same type of storm in the same place or very close to it.

In May 26, a storm developed close to the location of S1A but now as a spiral system traced by dust mixed with bright clouds (Fig. 6). From its morphology, we locate the rotation center of the spiral at 215°E and $72^0$N, inside the NPC, and we identify it again as a re-formed S1A. It covered a total area of ~$2.6 \times 10^5$ $km^2$ although a large portion of the polar cap is overcast with dispersed optically thin dust masses covering and hiding the bright polar ices. The length of the main arm of the spiral is ~2000 km (Fig. 6a, b, d) reminiscent of the band aspect of S1A in May 24 and 25, looking as if the band of 24–25 May had entered rotation. Within this arm, two bands can be distinguished, formed by an organized granular pattern with single cells with a size ~8–10 km in the head of elongated features with a length of 30–50 km, a width ~ 20 km and a separation of ~20–30 km (Fig. 6c, e, f). As before, the morphology of these worm-like structures suggests the drag of the dust from each head by the winds to form elongated tails with different wind direction in each band (Fig. 6f). The band closest to the pole suggests that the wind blows southeastward by about 30° with respect to the north-south meridian. In the second, most meridional band, the wind is directed southward, approximately parallel to the meridian. Outside the bands, the dust is dispersed over the pole by the winds where it mixes with water ice hazes, and no cellular texture is observed.

No storm was observed in this longitude sector in May 27 (Fig. 2), but in May 28, S1A re-formed again, this time as a compact-textured dust storm centered at 208°E and $61^0$N, occupying an area of ~$1.6 \times 10^5$ $km^2$ and partially penetrating the NPC (Fig. 7). The storm was tracked in images separated by 1.87 h that showed its rapid changes and vigorous dynamics (Fig. 7a and d). From the global displacement of S1A between these two images we deduce a south-east translation of the whole storm with a zonal velocity u = 10.6 $ms^{-1}$ and a meridional velocity v = −8.8 $ms^{-1}$ (horizontal velocity 14 $ms^{-1}$). The first image of the sequence shows that the main body of S1A consists of a cellular pattern, with each element elongated in the wind direction deduced according to global storm motion. The pattern is traced not only by the dust but in the north, within the NPC, it also manifests in the cloud field, where clouds mix with dust resembling the "pebbled" morphology described by Kulowski et al. (2017) and the "ruffled forms" described by Heavens (2017). In addition, the dust pattern shows a secondary organization in bands (six in total, arc shaped) oriented perpendicular to the wind direction (Fig. 7c). These arcs have lengths of ~320 km and a regular separation of ~40 km, suggesting that a wave phenomenon propagating in the wind direction could be involved in their organization.

In Table 3 we give the measurements of the sizes of a selected number of dust cells numbered 1–11 in Fig. 7b. They had a length of ~12 km and a width ~ 8 km with a mean cell-to-cell separation of 30 ± 8 km. As mentioned before, those similar cells are also observed in the cloud field (features 12–15 in Fig. 7b), but smaller in size, with a length of 5 km and a width of 3.3 km and the cell elongation in the wind direction. Mixture of condensate water ice clouds and dust in storms is a well-known phenomenon in the polar area (Malin et al., 2008; Heavens et al., 2019) and the fact that the same texture is shown by clouds and dust suggests that a common mechanism may be responsible for their formation.

The second image, taken 1.87 h later, shows the storm motion and its internal evolution (Fig. 7d–e). The area covered by the storm has grown to ~$1.7 \times 10^5$ $km^2$ but a large part of the cellular pattern has disappeared, and the dust is more uniformly distributed. A cellular pattern is still present in the north-west of S1A, but the cells are smaller, with lengths of ~5.5 km and widths of ~4.0 km, and a separation between centers of 17.4 ± 4.2 km. In some areas, the dust pattern resembles the ruffled morphology described by Heavens (2017). North West of S1A in Fig. 7d–e, we see cloud streets above the polar cap that resemble the "horizontal convective rolls" (HCR) observed on Earth (Houze, 2014; Markowski and Richardson, 2011). Both the dust cell pattern and the cloud streets are related and respond probably to organized convection in the Planetary Boundary Layer, as argued below.

We have used the highest resolution images from MARCI of the 28 May storm to measure the length of the shadows cast by different cells in the westward side of the storm. From the solar zenith angle obtained from ISIS tools and following the method given in Ordoñez-Etxeberria et al. (2020), we obtain an altitude of 6.7 ± 1.3 km. However, clouds in the southernmost regions seem somewhat higher, with an average altitude of 8.2 ± 1.1 km. As we show below, these values are similar to those retrieved from *VMC* images.

One day later, on May 29 we observed storm S1A at different local times, combining images from MARCI/MRO in Fig. 8 and VMC/MEX in Fig. 9. Fig. 8 shows that S1A exhibited again a spiral shape with center of rotation at ~195°E and 45°N. Unlike on May 26 (Fig. 6), the center of rotation was outside the polar cap, located equatorward, and the direction of rotation was cyclonic. This spiral evolved into a double arc-shape feature in just 1.87 h, and occupying a larger area ~ $1.4 \times 10^6$ $km^2$ than previously observed. The cellular texture is more irregular

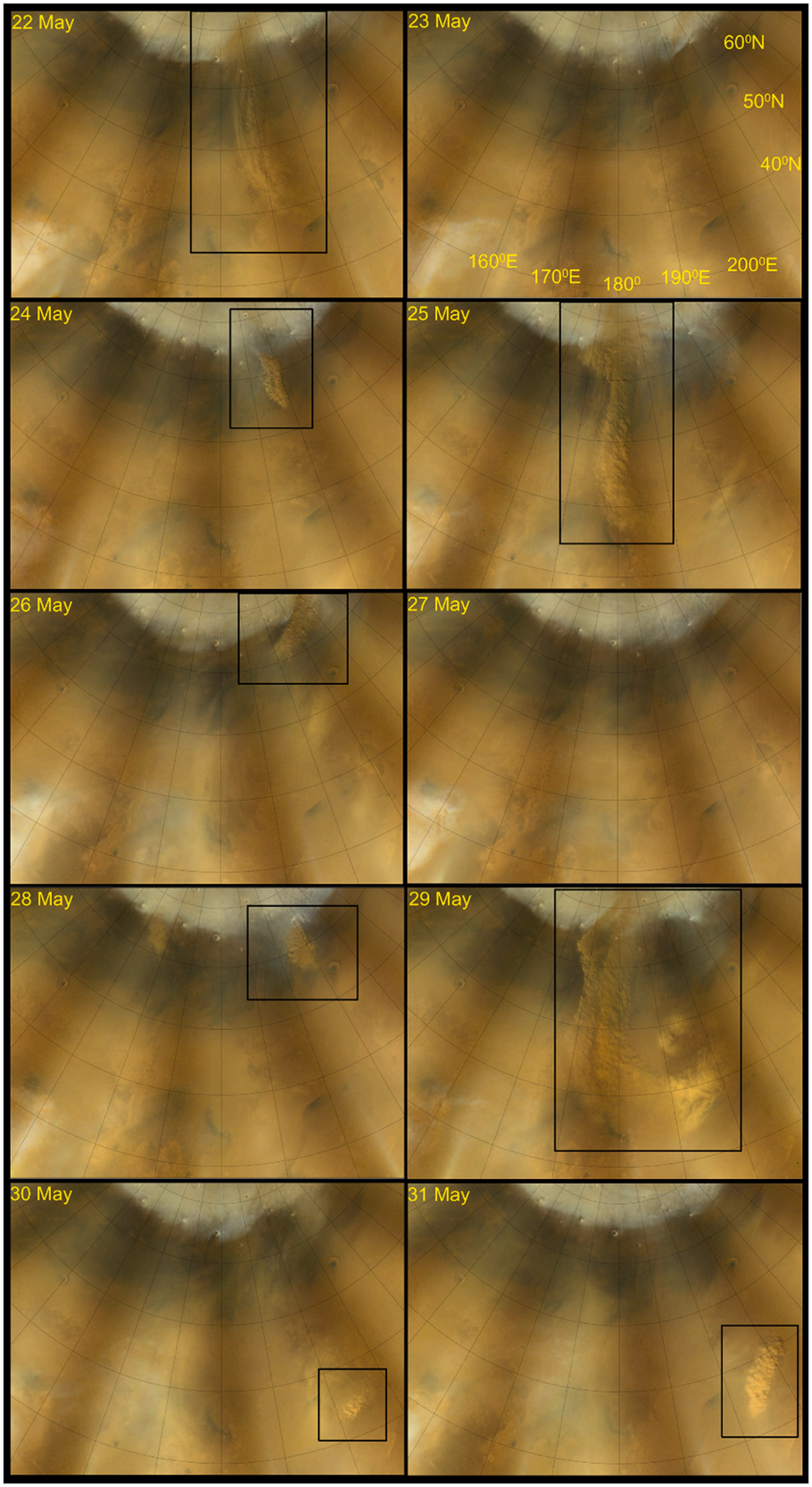


**Fig. 2.** Images of the dust storm S1A in polar map projections of the region where it evolved acquired with MARCI/MRO from May 22 to 31, 2019. The black rectangle frames the storm and note that no storm was observed in May 23 and 27.

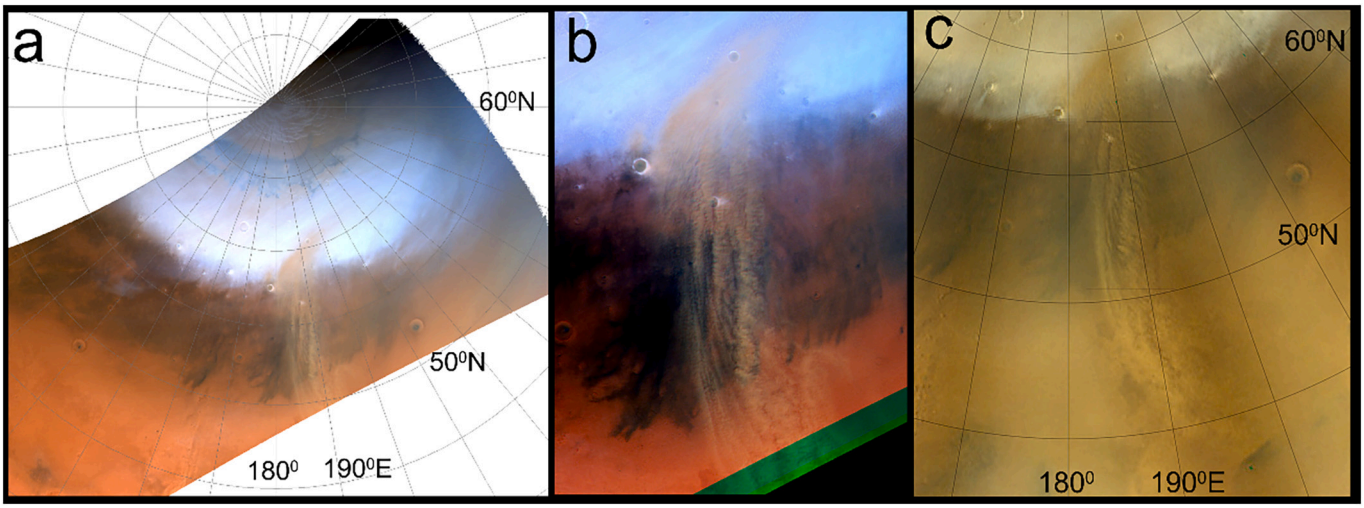


**Fig. 3.** Images of storm S1A acquired on May 22, 2019. (a)-(b) HRSC images at 08:36:22.5 UT: (a) navigated polar map projection showing S1A filamentary texture and (b) detail showing the three filaments with internal texture; (c) MARCI/MRO image taken at 09:09 UT showing the evolution of S1A in half an hour (The Martian Local Time LTST is 13:27 at the center of the storm).

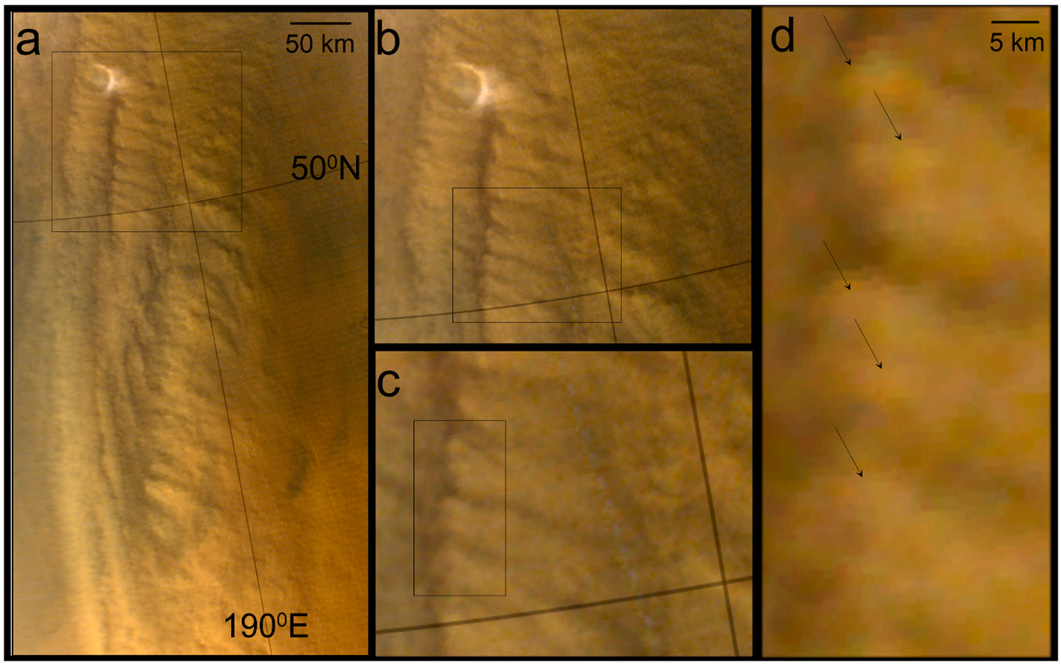


**Fig. 4.** Details in the image of storm S1A acquired on May 22, 2019 by MARCI/MRO (Fig. 3c) at 09:09 UT. Black rectangles frame the areas with successive magnifications, to highlight the shapes of features. Arrows in 3d indicate the compact-cell heads of the elongated structures in (a-c).

than in previous cases with numerous areas of dust clumps, but at the western edge of the band it is still possible to discern head cells with sizes 9–12 km and elongated tails of 30–50 km, oriented in the south-easterly direction (Fig. 8c–d).

The same day, VMC/MEX took images of the region between ~2.5 h and 3.5 h later than MARCI (Fig. 9). The double arm and the granular texture of S1A seen in Fig. 8 are still observed, but with cells having a larger size ~30–40 km (Table 3). This larger size could be due to a multi-cell structure, a combination of few closed cells, a pattern also observed in the higher resolution images of the storm in other days (Figs. 4–6). We have tracked the motion of some highlighted individual cells of the storm, obtaining eastward velocities in the range 18 $ms^{-1}$ to 40 $ms^{-1}$, with a mean value of $V = 26.2 \pm 6.9$ $ms^{-1}$ (Fig. 9e). The wind vectors show the northern cells moving northeast at about 35° whereas at the center they move southeast about 158°. This formed an arc-shape of the outer arm centered at ~56°N and 170°. From the displacement of the center of the storm in MARCI and *V*MC images (Figs. 8–9), separated by 5 h 35 min, we deduce a global eastward translation velocity of the spiral $V_{spiral} = 26.5$ $ms^{-1}$, the same as obtained from the individual cells motion.

VMC images have allowed us to retrieve the altitude (relative to ground) of the dust cells at the eastern limit of the storm during the evening, measuring the length of their shadow. We have applied the method described in Hernández-Bernal et al. (2021), which relies on the solar zenith angle on the top of the feature and takes into account the parallax due to the observation angle from the spacecraft. In our case, the solar zenith angle ranges between 75° and 83°, giving dust-top altitudes 5–8 km over the local topography.

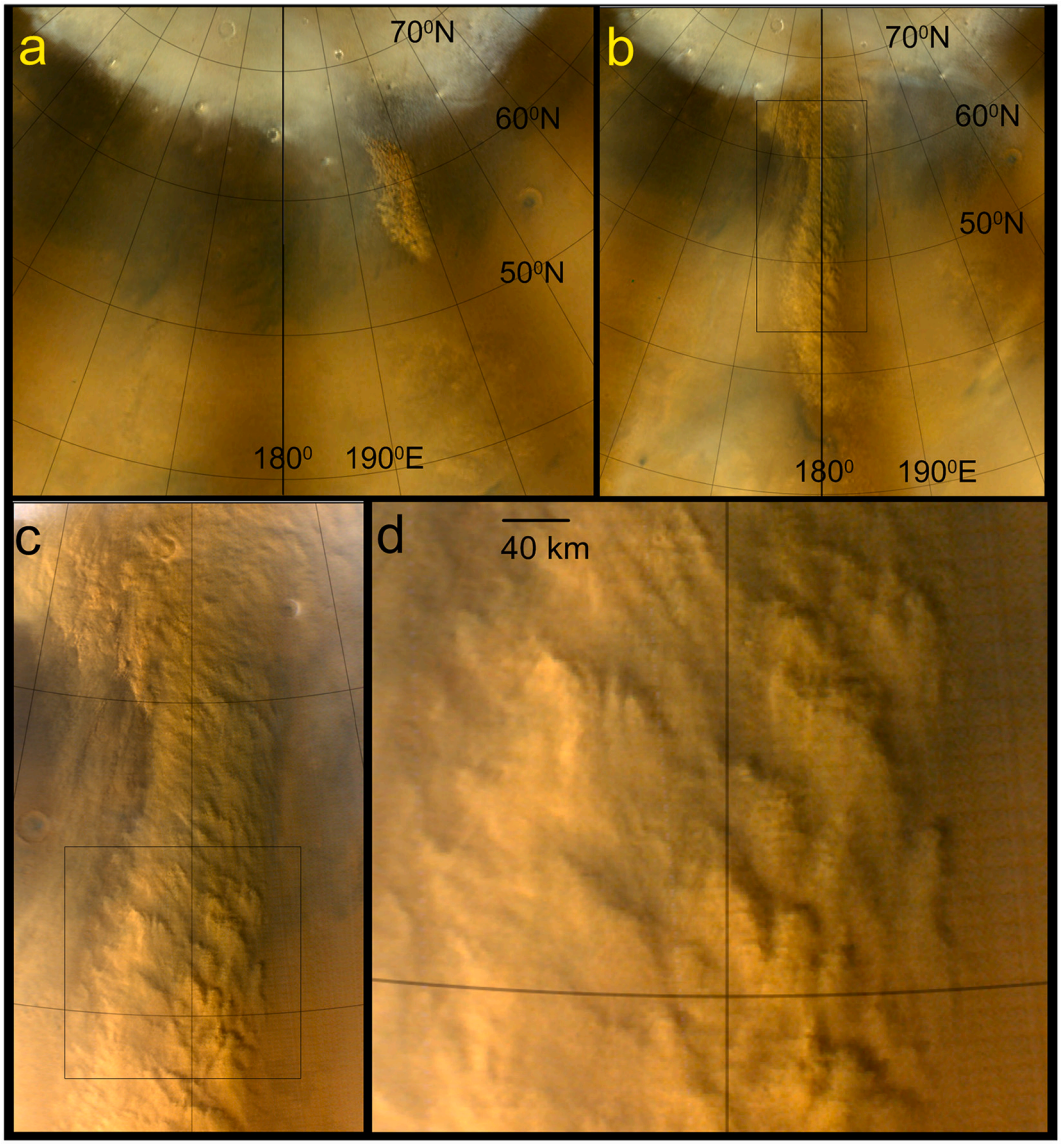


**Fig. 5.** MARCI/MRO images of storm S1A on two consecutive days: (a) 24 May (9:46 UT, LTST) and (b-d) 25 may (11:57 UT, LTST 13:36). Images (a) and (b) show changes in location and size, and (c-d) show details of the granular texture on 25 May.

Finally, Fig. 10 shows the decaying stage of storm S1A in the next 2 days (30 and 31 May), when it reduced to a small dusty area in the southern section of previous locations, at longitude ~205°E and latitude ~35°N. MARCI/MRO images show that the storm was still textured, with single cells of about 10 km in size but with organization in multi-cells of ~25–30 km.

## 5. Textured Storm 1B (S1B)

The second textured granular storm we study was observed with VMC in different image sequences in 4–6 June (Ls = 34°) (Fig. 11). It was a compact dust system in Arcadia Planitia, consisting of a pattern of pebbled-puffy cells, covering an area ~ $1.8 \times 10^5$ km$^2$ and located over the edge of the NPC at about 68°N in the longitude range 150°E - 170°E. Since S1B formed close to the location of S1A, it is reasonable to assume that its formation mechanism is similar. Most prominent cells, which stand out for their contrast, have lengths of ~23 km and width of ~17 km, giving a length/width ratio of 1.3, similar to that of storms S1A (Table 3). We tracked the motion of selected cells in the image sequence of June 4 (Fig. 11a, b), obtaining a mean velocity $< V \geq 25.1 \pm 10.6$ ms$^{-1}$. Winds are stronger in the northern part of the storm (latitudes 68° – 72°N), reaching $<V> \sim 45$ ms$^{-1}$, and slower in the southern part with $<V> \sim 13$ ms$^{-1}$, indicative of an intense meridional wind shear.

We also have retrieved the altitude of some dust cells by measuring their shadows as seen by VMC at the eastern edge of the storm at local evening, using the method described above for VMC altitude retrievals (Hernández-Bernal et al., 2021). We find cell altitudes of 7–11 km over the local ground.

## 6. Irregular and flushing storms (S2, S3)

Simultaneously to the development of storms clusters S1A and S1B, other visually different kind of dust storms developed at the edge of the NPC but in other longitude sectors (Fig. 1). Attending to their different dust distribution, we classified them as irregular storms (identified as S2) and arc-like or "flushing" storms (identified as S3).

In Fig. 12 we show examples of the irregular dust storms systems observed in 25–27 May. They displayed some large filaments with a zonal length of 2100 km and meridional extension of about 900 km (Fig. 12b, c). If we assume that the storms observed those days are the same storm, tracking the motion of the dusty area gives a translation eastward velocity of 12.5 ms$^{-1}$. In spite of their irregular shape, the

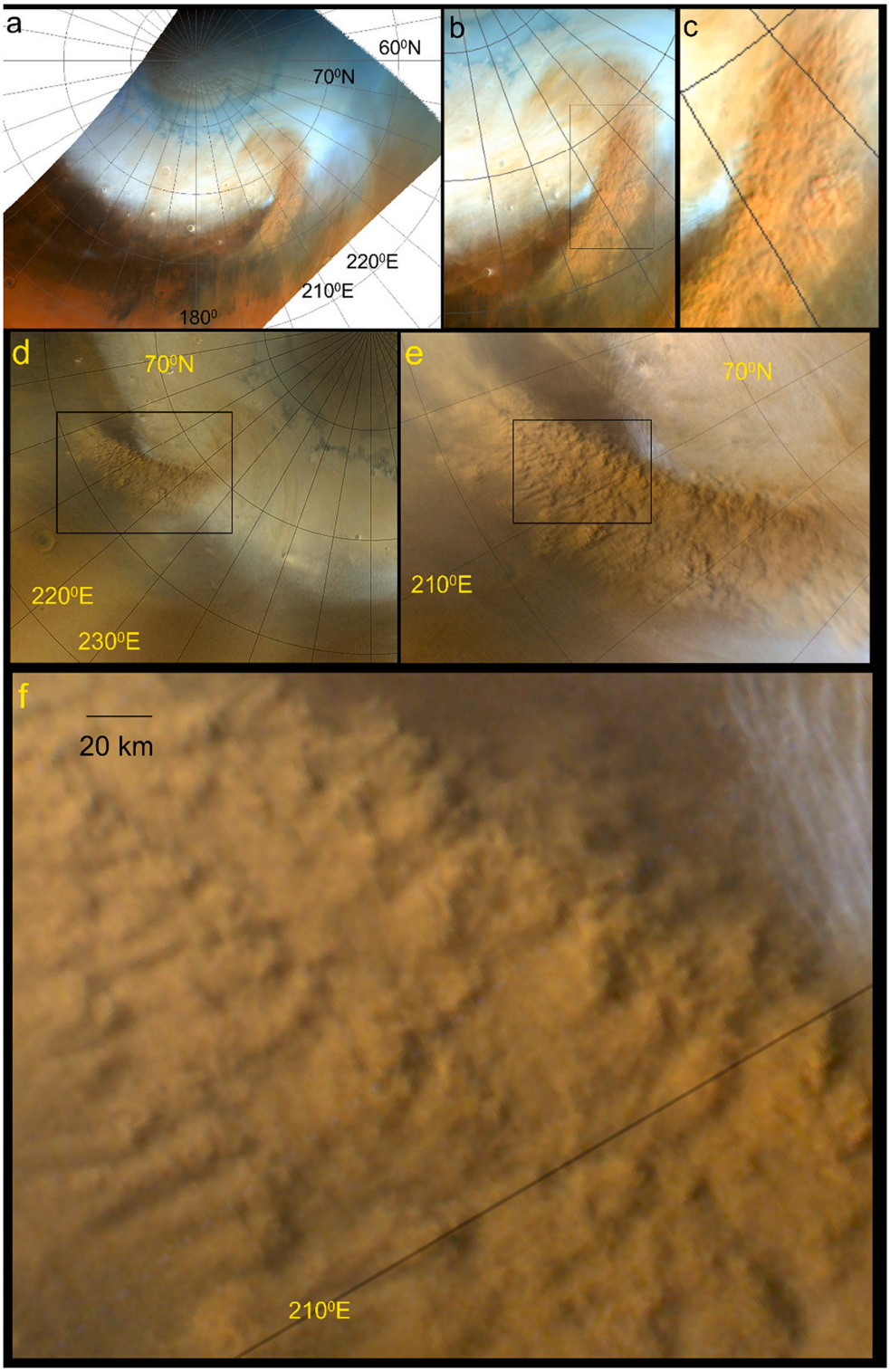


**Fig. 6.** Images of storm S1A on May 26, when it developed into a spiral morphology,: (a) HRSC/MEX polar map projection at 10 h 16 min 18 s UT (LTST 13 h 35 min); (b) and (c) successive zooms of the spiral and the cellular pattern in the dusty arm; (d) Image from MARCI/MRO obtained 8 min later at 10 h 24 min UT; (e) and (f) zooms of (d) showing in detail the cellular pattern in the dusty arm.

images of May 26 and 27 show that the more compact and denser areas (longitude 320°E in Fig. 12d, longitude 20°E in Fig. 12e) also exhibit some granular texture, similar to storms S1A and S1B. This suggests that the same mechanism of cell formation took place in these regions.

Arc-shaped and flushing storms have been previously described in the literature (Wang and Fisher, 2009; Guzewich et al., 2015; and Sánchez-Lavega et al., 2018a). During the studied period (25 May – 9 July, Ls = 30°-50°) we observed the presence of several such disturbances evolving in the longitude sector 315°E-330°E in Acidalia Planitia (Fig. 13). The arc-shaped structures extend preferentially outward from the NPC and propagate in the region not covered by the polar ices. The arcs have a length of ~2350 km and a width of ~250 km. From the

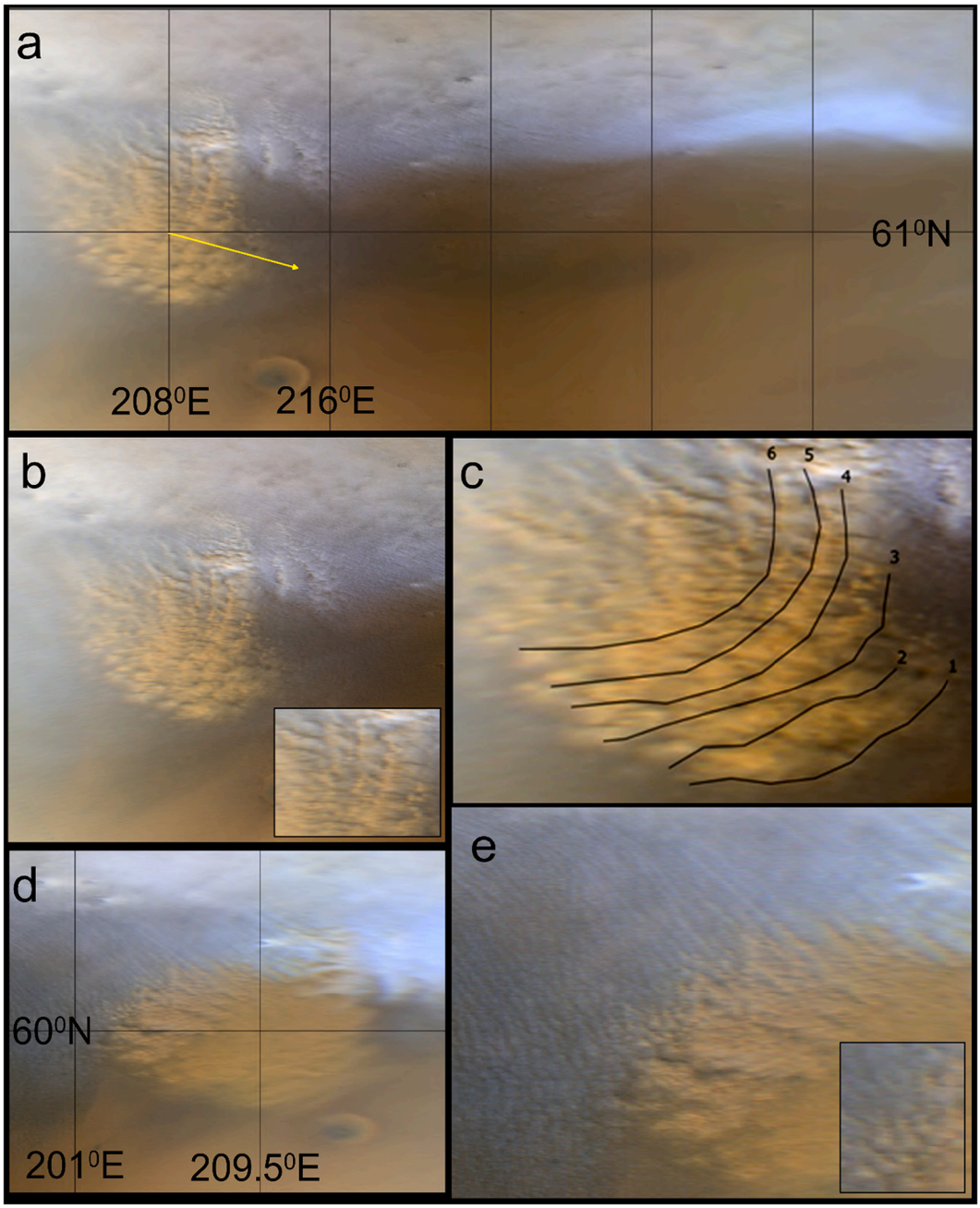


**Fig. 7.** MARCI/MRO images of S1A on May 28: (a) Navigated map projected image obtained at 11 h 01 min 48 s UT (LTST 12.5 h). The yellow arrow marks the wind direction; (b) Same as (a) but showing details of the cellular pattern (see inset); (c) Same as (a) this time showing the banded distribution; (d) Image of S1 obtained at 12 h 53 min 58 s UT (LTST 14.5 h) showing the dust dispersion and the disappearance of the cellular pattern; (e) Same as (d) showing the details of the storm and cloud texture at the northern edge with details of the cells in the inset. (For interpretation of the references to colour in this figure legend, the reader is referred to the web version of this article.)

image series corresponding to July 9 (Fig. 13c illustrates one of these images) we measured an outward expansion of the arc with a velocity of 29 $ms^{-1}$. No granular texture was observed in the interior of these arcs.

The morphology of this kind of storms, with curved arcs and filamentary shapes, suggests some development of cyclonic vorticity, perhaps less intense than that involved in the development of the spiral formations mentioned in Section 5 (Figs. 6 and 8).

## 7. Dynamical mechanisms

The morphology shown by the dust storms and their large and small-scale organization, suggests the intervention of different dynamic instabilities. These instabilities, as they develop at the edge of the NPC, evolve in part in the north, within the NPC, where they become visible when traced by water ice clouds and dust. However, they mainly extend to the south, where they become visible only by the dust they lift. The primary mechanism behind the disturbances is the strong meridional temperature gradient that occurs between the ice-occupied regions in the NPC and the soil where CO2 ice has already evaporated (Figs. 14a). On a large synoptic-scale, the spiral and filamentary formations (banded structures) are the result of a baroclinic instability as proposed in previous works (Barnes et al., 1993; Wang and Ingersoll, 2002; Wang et al., 2005; Tyler Jr. and Barnes, 2005; Hinson, 2006; Hinson and Wilson, 2021; Sánchez-Lavega et al., 2018b). The surface winds and their

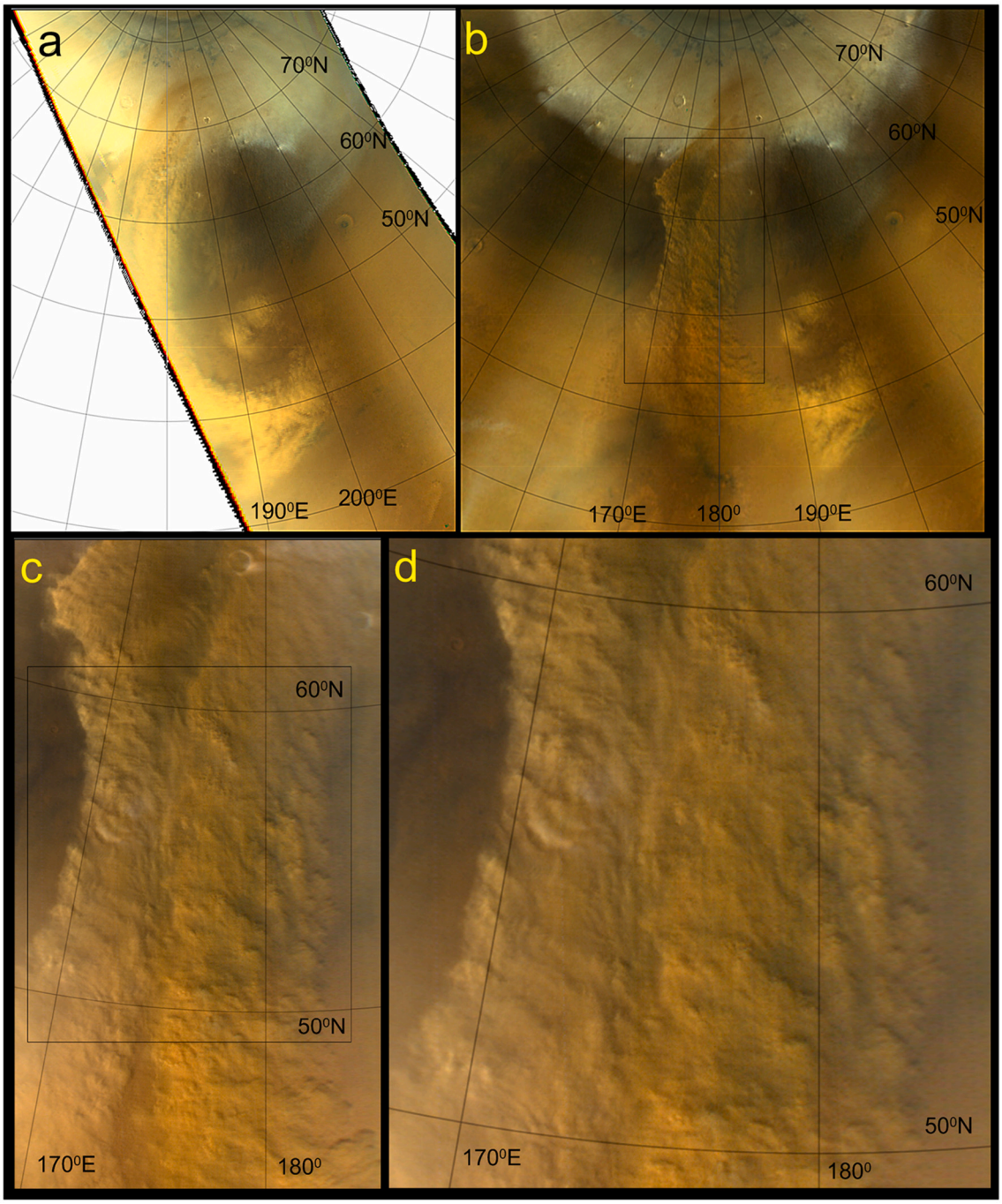


**Fig. 8.** MARCI/MRO images of S1A on May 29: (a) Navigated and map-projected image obtained at 13 h 12 min 40s UT (LTST 13.3 h); (b) Image obtained at 15 h 04 min 52 s UT (LTST 15.1 h); (c-d) Enlargements of the rectangular areas to show in detail the cellular pattern in the dusty arm.

stresses have a maximum in the longitude sector from 180°E to 270°E (Fig. 14b, c) where storms S1 evolved, indicating their important role in dust lifting (Newman et al., 2002; Guzewich et al., 2015). On the mesoscale, we propose that the granular cell-like features are due to convective instability triggered by dust heating.

Fig. 14b, c also strongly suggests the presence at this season of a jet streak. When comparing with the tracks in Fig. 1, it seems possible that storms S1 and S2 formed in the entrance region, while S3 storms tend to form in the exit region. This is an aspect that merits a further future independent study.

### 7.1. *Baroclinic instability*

Here we explore the baroclinic instability conditions for the location of the spiral storms S1A in Fig. 8 (longitude 195°E, latitude 45°N) at the date and time of its detection (29 May 2019 at 13:12 UT, Ls = 31.8°, LTST = 13.3 h). We use physical parameters deduced from the MCD-LMD model Version 5.3 (Forget et al., 1999; Millour et al., 2018) under the climatological minimum solar scenario. We propose these spirals are produced by baroclinic instability with cold fronts forming the bands and filaments, and the associated winds, the tails in the cells.

Fig. 15 shows the meridional and height distribution of the temperature and wind velocity at this location and time, which imply baroclinic conditions in the atmosphere. The Rossby number corresponding

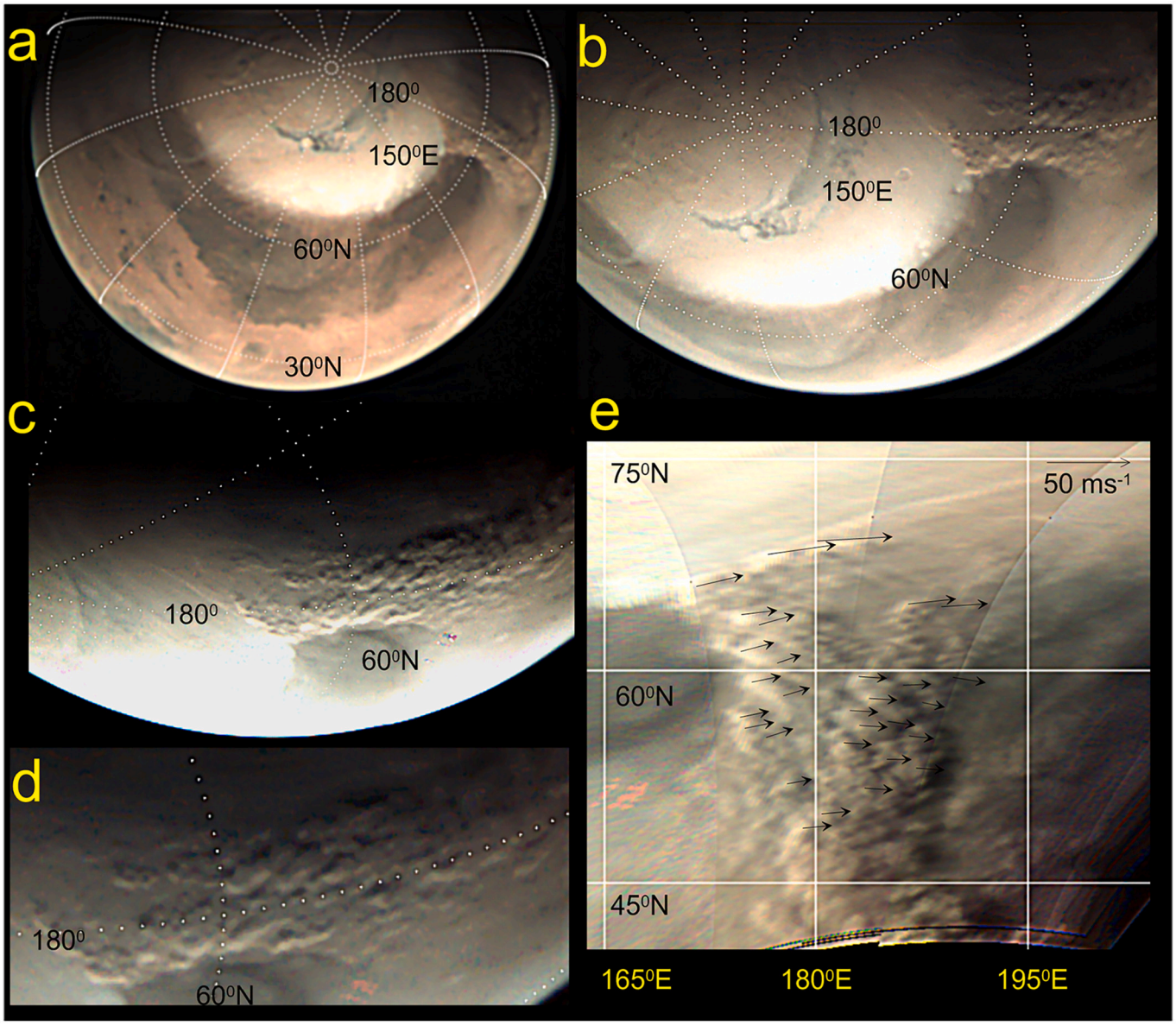


**Fig. 9.** VMC/MEX images of S1A on May 29: (a) 17 h 43 min 52 s UT; (b) 18 h 27 min 09 s; (c) 18 h 47 min 10 s; (d) 18 h 47 min 58 s; (e) map projection at 18 h 46 min with superimposed wind vectors retrieved from the track of individual feature motions. LTST of the images ranges between 16 and 18 h.

to the zonal jet and storm motion is $R_0 = U/fL \sim 0.08$–$0.18$ ($f = 1.1 \times 10^{-4}$ s$^{-1}$, $U$ = 18–40 ms$^{-1}$ as measured, $L \sim 2000$ km for the jet meridional extent) indicating geostrophic conditions. From the model output, the meridional temperature gradient has a peak value $\partial T/\partial y \sim 25$ K/1000 km at heights $z \sim 2$–5 km and a vertical shear of the zonal wind $\partial u/\partial z \sim 55$ ms$^{-1}$/16 km (3.4 ms$^{-1}$/km) at about 68°N, close to thermal wind balance $\partial u/\partial z = -(g/fT)\partial T/\partial y$ (see e.g. Sánchez-Lavega, 2011). An important parameter to characterize the horizontal scale of the baroclinic instability is the Rossby deformation radius defined as $L_D = NH/f$, where $N$ is the Brunt-Väisälä frequency $N^2 = (dT/dz + g/C_P)g/T$ and $H = R^*T/g$ the scale-height. Using $C_p = 780$ Jkg$^{-1}$ K$^{-1}$, $R^* = 192$ J kg$^{-1}$ K$^{-1}$, $g = 3.72$ ms$^{-2}$ and taking the temperature values from the MCD, we find for the altitude range 2–10 km, $N \sim 0.011$ s$^{-1}$, $H = 10.5$ km and $L_D = 1150$ km.

We assess the properties of the spiral system S1A using the Eady model that assumes constant vertical wind shear and $\beta = df/dy = 0$ (Holton, 2004). The growing rate of the most unstable mode is $\sim (f/N)(\partial u/\partial z) = \sim 3.5 \times 10^{-5}$ s$^{-1}$ (corresponding to time-scales ~8 h). From Fig. 8, spiral S1A on 29 May had a zonal length of 30° ($L_x = 1150$ km) and a meridional extent of about 33° ($L_y = 1955$ km), and then $L_D \sim L_x \sim 0.6\, L_y$. For waves with equal zonal and meridional wavenumbers ($k = \ell$), the wavelength corresponding to the maximum growth rate is $L_{\mathrm{Bclin}} \sim (3.9$–$5.5)\, L_D \sim 4485$–$6325$ km (Lin, 2007; Vallis, 2006). The phase speed of these waves is $c_r = (H/2)(\partial u/\partial z) \sim 35$ ms$^{-1}$ and the corresponding translation zonal velocity relative to the mean flow is $U_{\mathrm{vortex}} = U_0 - c_r$. From our measurements we have $U_{\mathrm{vortex}} \sim 15$ ms$^{-1}$ and then $U_0 \sim 50$ ms$^{-1}$. According to the wind speeds predicted by the model and presented in Fig. 15, this velocity corresponds to a disturbance altitude $z \sim 10$ km.

We assume the spiral system to be in gradient wind balance, as has been observed in other baroclinic spiral systems on Mars (Hunt and James, 1979; Sánchez-Lavega et al., 2018b). Then the tangential rotation velocity $V_T$ obeys the equation

$$\frac{V_T^2}{R} + fV_T = -\frac{1}{\rho}\frac{dP}{dr} \tag{2}$$

Taking for the radius of the vortex $R \sim (L_x + L_y)/2 - 775$ km, a mean density $\rho = 0.025$ kg m$^{-3}$ and $\partial P/\partial r \sim 5$ Pa/100 km as observed in other

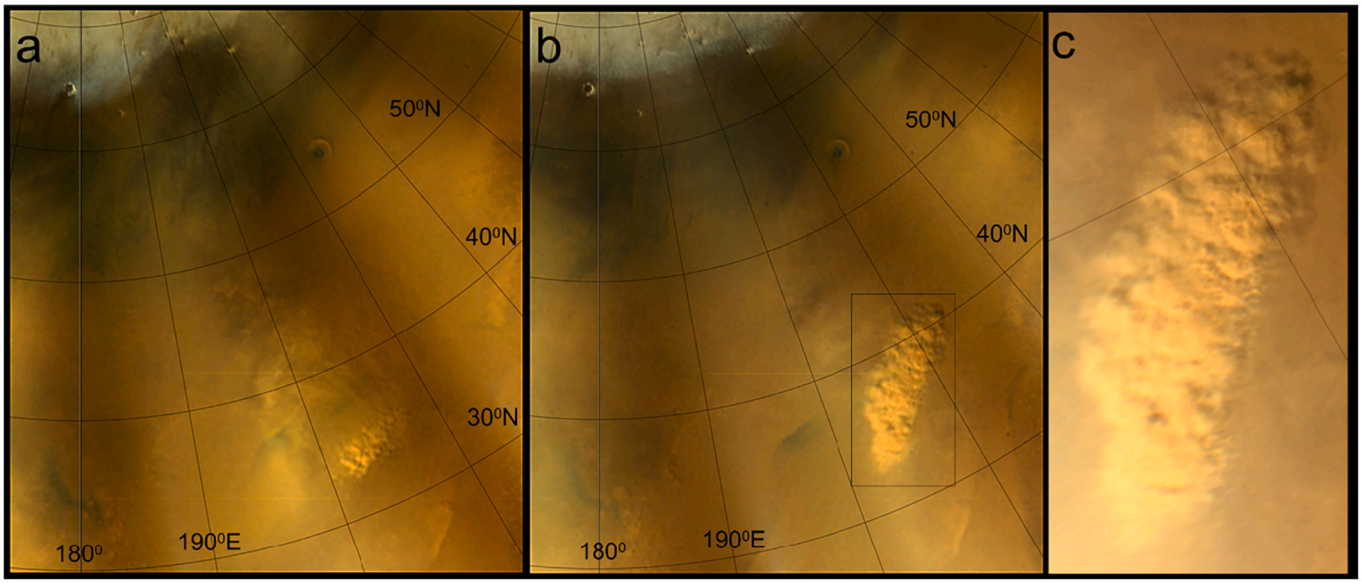


**Fig. 10.** MARCI/MRO images of decaying storm S1A: (a) May 30 at 13 h 31 min UT (LTST 13 h 17 min); (b) Image obtained on May 31 at 13 h 49 min UT (LTST 13 h 17 min); (c) Enlargement of image (b) to show the cellular pattern within the storm.

**Table 2**
S1A filaments.

| Filament | Length (km) | Width (km) | Separation (km) |
|---|---|---|---|
| 1 | 950 | 85 | 39 (1–2) |
| 2 | 656 | 58 | 35 (2–3) |
| 3 | 497 | 25 | – |

Note: The filaments are numbered from West to East (left to right in Fig. 3).

**Table 3**
Cell properties in storm S1A (22–31 May) and S1B (4–6 June).

| Date | Camera | <L> (km) | <w> (km) | <L>/<w> | N | S1A shape |
|---|---|---|---|---|---|---|
| May 22 | MARCI HRSC | 7.5 ± 2.5 | 6 ± 2 | 1.25 | 10 | Band |
| May 25 | MARCI | 11.6 ± 3.2 | 9 ± 3 | 1.3 | 22 | Band |
| May 26 | MARCI HRSC | 9.5 ± 3.0 | 8 ± 2 | 1.2 | 28 | Spiral |
| May 28 | MARCI | 11.6 ± 6.5 | 7.6 ± 4.1 | 1.5 | 20 | Compact |
| May 28 | MARCI | 5.5 ± 1.5 | 4.0 ± 1.3 | 1.4 | 8 | Compact |
| May 29 | MARCI | 10.5 ± 2 | 7 ± 2 | 1.5 | 10 | Spiral-Band |
| May 29 | VMC | 39.1 ± 3.9 | 30.8 ± 7 | 1.3 | 9 | Band |
| May 31 | MARCI | 11.5 ± 3 | 8.5 ± 2 | 1.3 | 36 | Band-Compact |
| June 4 | VMC | 29.5 ± 6.1 | 23.7 ± 5.5 | 1.26 | 19 | Compact |
| June 6 | VMC | 23.2 ± 7.0 | 17.0 ± 7 | 1.3 | 7 | Compact |

vortices, the tangential velocity is $V_T \sim 25$ ms$^{-1}$ (18 ms$^{-1}$ for pure geostrophic conditons).

According to the temperature and rotation velocity predicted by the model, the large dust arm (with a clearly double structure on May 29), is likely to be formed by a cold front with low temperatures inward of the spiral arm.

### 7.2. Dry convection

Dry convection on Mars occurs at a local-scale in the Planetary Boundary Layer and surface layer during the hours of daily maximum insolation heating with the convective mixed layer reaching typically altitudes of ~6 km (Read et al., 2015). Properties of convective instability driven by surface heating on Mars were studied by Odaka et al. (1998) and Odaka (2001) using a two-dimensional anelastic model. They found that at noon convective motions reach on Mars altitudes up to 10 km with maximum velocities of 30 ms$^{-1}$. Newman et al. (2002) performed simulations of regional dust storms with the dust being radiatively active, to enhanced the local heating of dust-laden air in daytime. The extra heating leads to enhance lifting in convective plumes, which are able to inject dust up to altitudes of 30–40 km. Heavens et al. (2011) used a one-dimension model to explore the velocities and altitudes reached by thermal plumes. Spiga et al. (2013) used a three-dimensional mesoscale model to show that enough convective energy can be stored by the dust to generate deep plumes able to transport dust up to altitudes of 30–50 km, in the so-called "rocket dust storms". Heavens et al. (2019) called this phenomena "dusty deep convection" (DDC) and their new calculations showed that vertical dust streamers can deposit dust at high altitudes (up to 90–100 km).

Here, we propose that the cells observed in the arms of the dust storm clusters S1A and S1B can be the result of dry convection, when parcels of air with sufficiently high concentrations of dust are heated by the solar radiation, generating buoyancy relative to the environment and ascent (Read et al., 2015). The vertical shear of the wind blowing over the dust in the front organizes the convective pattern and forms the downwind tails of the cells.

### 7.3. One dimensional dry convection model

A first estimation of the updraft velocities can be obtained from the Convective Available Potential Energy (CAPE, in Jkg$^{-1}$), given by Read et al. (2015).

$$CAPE = \frac{w_{\max}^2}{2} = \int_{\substack{Storm \\ size}} g\left(\frac{T_p - T}{T}\right) dz \quad (3)$$

where $w$ is the vertical velocity, $T$ and $Tp$ are the ambient and parcel

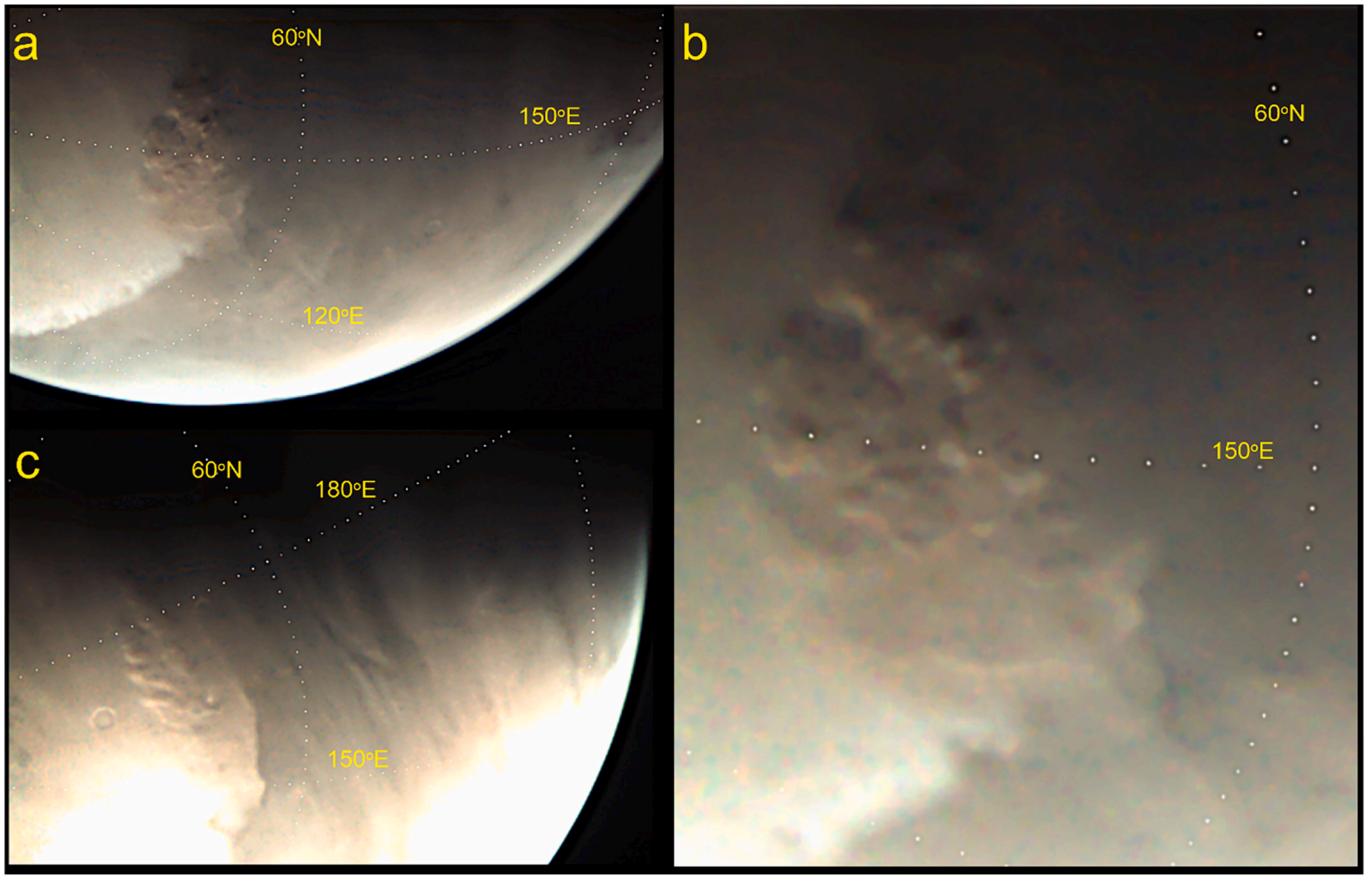


**Fig. 11.** VMC/MEX images of S1B: (a) Image obtained in June 4 at 00 h 26 min 41 s UT (LTST 17.3 h), (b) Enlargement of the previous image to show the cells and their shadows; (c) Image obtained in June 6 at 01 h 15 min 33 s (LTST 18.6 h).

temperatures. The maximum velocity of the convective updrafts is then given by

$$w_{\max} \approx \sqrt{2g\left(\frac{\Delta T}{T}\right)\Delta z} \tag{4}$$

with $\Delta T = T_p – T$. For a vertical extent $\Delta z = 1$ km, a contrast in temperature $\Delta T = 5$ K and $T = 200$ K, we get $w_{\max} \sim 14$ ms$^{-1}$.

To estimate the height reached by the dust, we consider the momentum equation for a dusty heated dry atmospheric parcel (Sánchez-Lavega, 2011; Houze, 2014):

$$w\frac{dw}{dz} = \underbrace{g\left(\frac{T_p - T}{T}\right)}_{\substack{\text{Buoyancy}\\ \text{Force (dry ambient)}}} + \underbrace{g\frac{\partial \pi_D}{\partial P}}_{\substack{\text{Perturbation}\\ \text{pressure Force}}} \underbrace{- C_D\frac{w^2}{r_0}}_{\text{Drag}} \underbrace{- \frac{1}{m}\frac{dm}{dz}w^2}_{\text{Entrainment}} \underbrace{- g\ell_C}_{\substack{\text{Dust}\\ \text{weight}}} \tag{5}$$

where $w$ is the vertical velocity, $\pi_D$ the dynamic pressure, $C_D$ a drag coefficient, $m$ and $r_0$ the parcel mass and size and $\ell_C$the dust mass content of the parcel relative to parcel total mass.

Using pressure as a vertical coordinate we rewrite (5) as

$$\frac{dw^2}{dP} = -\frac{2}{\rho}\left(\frac{T_p - T}{T}\right) - \frac{2}{\rho}\frac{\partial \pi_D}{\partial P} + \frac{2\,C_D}{\rho g\, r_0}w^2 - \frac{2}{m}\frac{dm}{dP}w^2 + \frac{2}{\rho}\ell_C \tag{6}$$

Others effects affecting the buoyancy of the parcel, as the presence of water ice clouds or latent heat release are not considered here (Heavens et al., 2019).

In order to solve the full equation, we approximate the terms on the right of Eq. (6) as follows:

The ambient temperature is the profile retrieved from the MCD-LMD for the conditions in the case of the storm S1, and in a first approximation, the temperature of the parcel is considered to evolve adiabatically.

The friction force on the ascending parcel is parameterized using a drag coefficient $C_D$ that depends on the shape of the ascending parcel (the form coefficient) and of the velocity (Kundu and Cohen, 2008). It can be written in terms of the Reynolds number $Re = \frac{\rho L w}{\eta}$, where $L$ is a characteristic length transversal to the direction of motion and $\eta$ is the viscosity.

Entrainment is a complex phenomenon, and here we use a simple parameterization following the approach used in the study of cumulus clouds on Earth and other planets (Simpson, 1971; Houze, 2014)

$$\frac{1}{m}\frac{dm}{dP} = -\frac{gP}{R^* T}\frac{\alpha}{r_0} = X \tag{7}$$

where $\alpha$ is a parameter empirically determined from studies of laboratory plumes (Stommel, 1947).

The weight of the dust excess in the parcel $\ell_C$ is based on the dust content in the atmosphere as predicted by the MCD.

The perturbation pressure can be written as

$$\frac{\partial \pi_D}{\partial P} = \frac{1}{2}\frac{\partial \rho}{\partial P}w^2 + \frac{1}{2}\rho\frac{dw^2}{dP} \tag{8}$$

From the equation of state $\rho = \frac{P}{R^* T}$ and hydrostatic balance $\frac{dP}{dz} = -\rho g$ we have

$$\frac{\partial \rho}{\partial P} = \frac{1}{R^* T} + \frac{1}{gT}\frac{\partial T}{\partial z} \tag{9}$$

and substituting (7), (8) and (9) in (6), and rearranging terms, we get

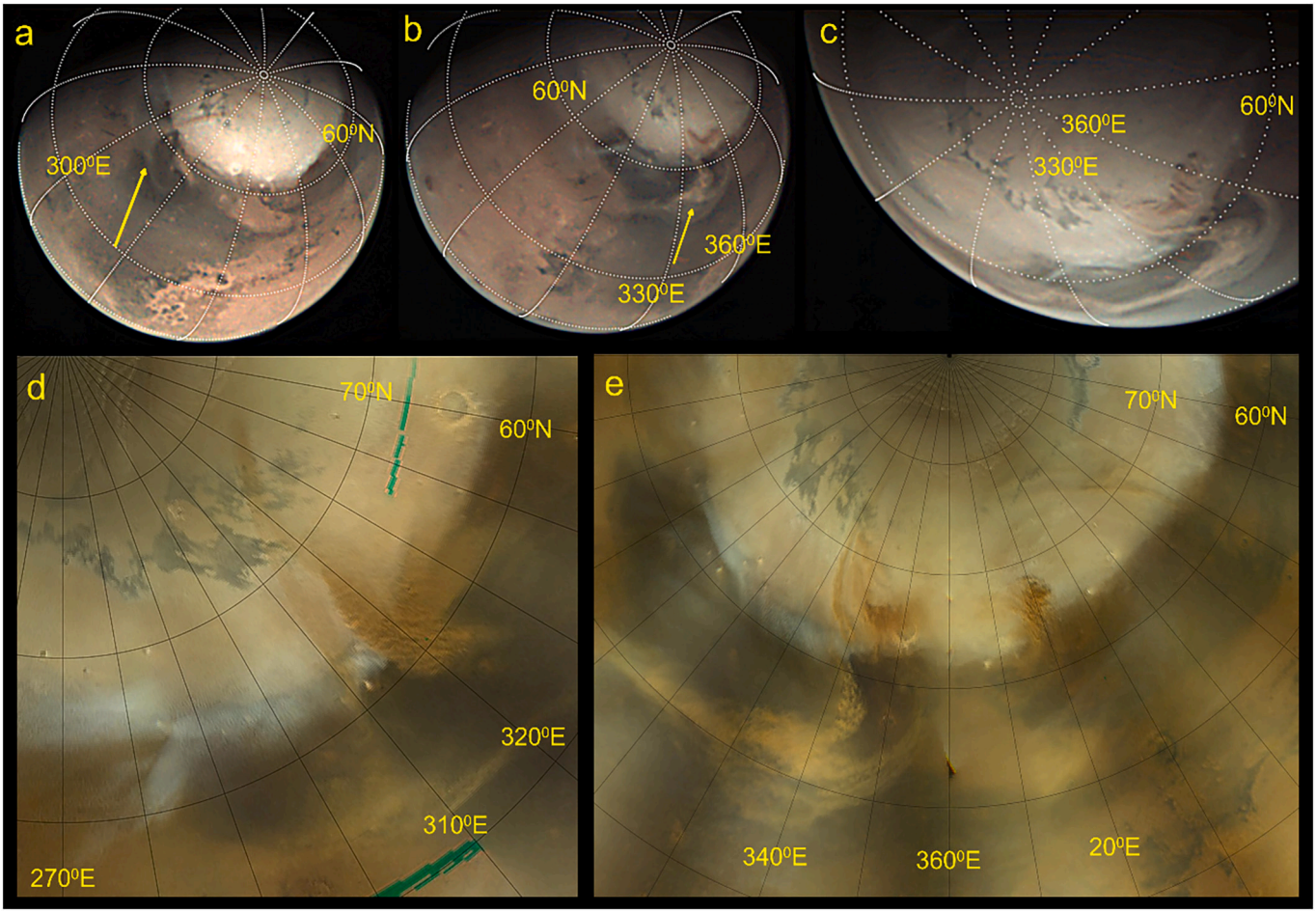


**Fig. 12.** Images of storms of type S2. VMC/MEX: (a) 25 May (22 h 09 min 50 s UT, LTST = 7.9 h; Ls = 30.3°); (b) 27 May (01 h 55 min 20 UT, LTST = 13.1 h; Ls = 30.8°); (c) 27 May (03 h 37 min 06 s UT, LTST = 15 h; Ls = 30.8°). MARCI/MRO: (d) 26 May (02 h 55 min UT, LTST 13 h 31 min); (e) 27 May composed image, left part obtained at 01 h 21 min UT (LTST 13 h 27 min on storm at 345°E), right part obtained at 23 h 48 min UT (LTST 13 h 12 min on storm at 20°E).

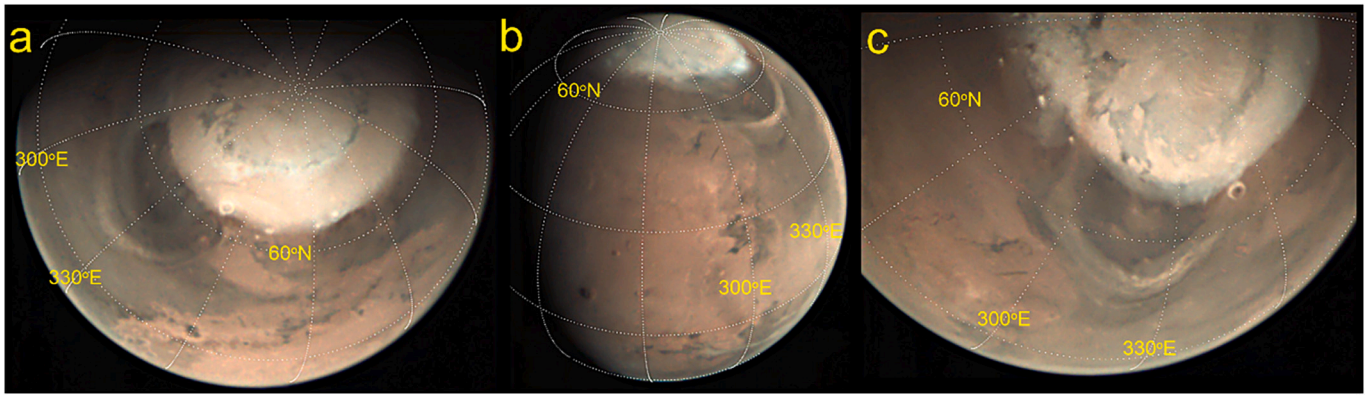


**Fig. 13.** VMC/MEX images of storms of type S3 (arc-shape or flushing): (a) 3 June (02:28:53 UT, LTST = 8.4 h; Ls = 34°); (b) 5 July (01:46:55 UT, LTST = 11.2 h; Ls = 48.4°); (c) 9 July (05:03:58 UT, LTST = 10 h; Ls = 50.2°).

$$\frac{dw^2}{dP} = \underbrace{-\frac{R^*}{P}\left[\left(T_p - T\right) - T\ell_C\right]}_{A(P)} \underbrace{-\left[\frac{1}{2P}\left(1 + \frac{R^*}{g}\frac{\partial T}{\partial z}\right) + X - \frac{R^* T C_D}{P g r_0}\right]}_{B(P)} w^2 \tag{10}$$

We solve (11) numerically to get the vertical velocity $w$ as a function of altitude for different values of the parameters within the ranges in Table 4. The parcel initial temperature excess relative to the environment is denoted as $\Delta T_0$ and its range of values are taken following the calculations of the heating and cooling rates given by Spiga et al. (2013) and Heavens et al. (2019). Typical values of the heating rates due to shortwave solar radiation are ~15–20 K per Martian hour for dust mass mixing ratios of $5 \times 10^{-5}$. The environment vertical temperature profile is taken from the Mars Climate Database in the region and date of the storm development. In a first approach, the parcel temperature is assumed to follow a dry adiabatic profile ($dT/dz = -g/$

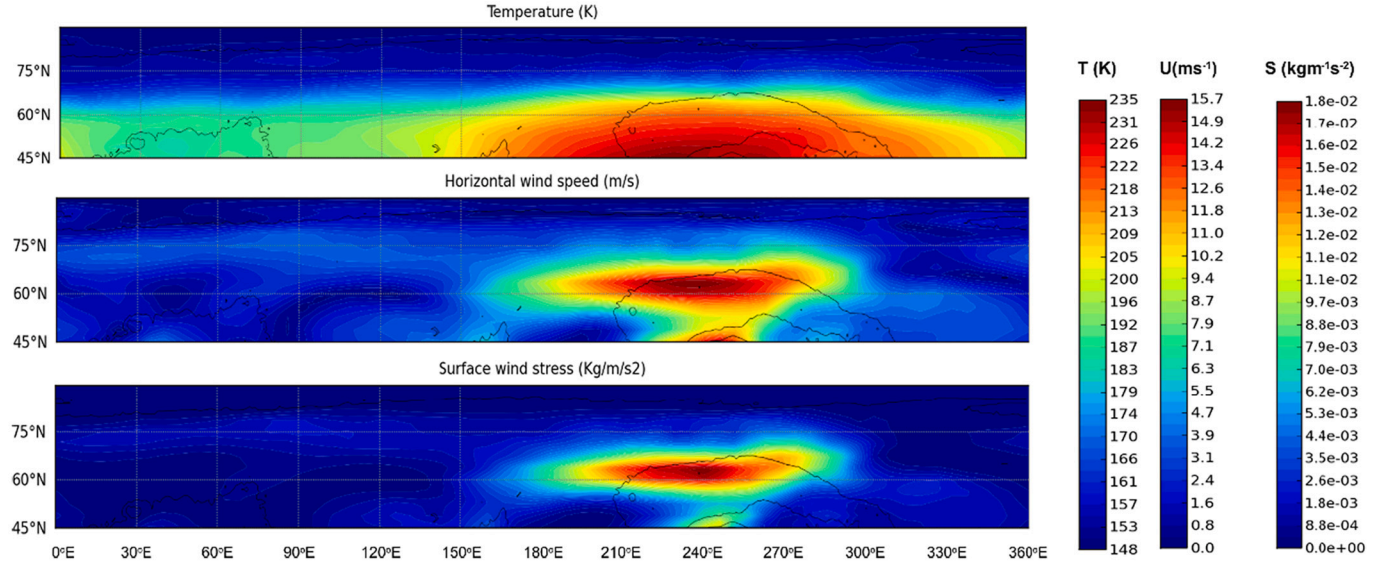


**Fig. 14.** Map of the surface temperature, horizontal wind and surface wind stress for 28 May 2019 at 11:01:48 UT (Ls = 31.3°) corresponding to the image in Fig. 5a, according to the Mars Climate Database (MCD-LMD).

*Cp*). The parcel temperature relative to the environment (the parcel buoyancy) is positive and impulses the parcel ascent. Panel a-c of Fig. 16 show examples of the vertical velocity profiles and maximum altitudes reached by thermals. We find that the peak velocity is at 2–5 km altitude with maximum ascending velocities $w_{max} \sim$ 20–35 ms$^{-1}$. The parcel top altitude is 12–15 km in agreement with previous similar studies (Heavens et al., 2011).

The top altitudes relative to the ground that we have derived from the cells shadows, ~ 6–11 km is below the top altitudes of ~15 km predicted by the 1D-parcel model under reasonable values of the parameters. Lower top altitudes can occur in the model if the parcel does not follow a dry adiabat during its ascent but interchanges heat (Q) with the environment. We parameterized this rate of heat exchange to be proportional to the size (or weight of the parcel) such that the parcel temperature gradient can be written as

$$\frac{dT}{dz} = -\varepsilon \frac{g}{C_p} \tag{11}$$

We found that using $\varepsilon = 2$ the speed of ascent of the parcel is suitably reduced so that it reaches a top altitude ~6–10 km in the range of what is observed (Fig. 16d, e).

### 7.4. Cell anisotropy

All our measurements of cell sizes show an anisotropy in their length to width ratio with a value $r$ = 1.3–3.0 (Table 3). The direction of cell elongation coincides reasonably well with the direction of motion of the storm and of its elements. One possible explanation is that the elongation is produced by a vertical wind shear with higher values of the velocity at the top of the cell than at its base. Assuming that the wind speed at the cell top depends linearly with the anisotropy factor $r$, we have.

$$\frac{\partial u}{\partial z} \approx \frac{< V > (r-1)}{h} \sim 4 \text{ ms}^{-1} \Big/ \text{km} \tag{12}$$

where we have taken from our measurements a zonal wind $< V > \sim$ 20 ms$^{-1}$ at cell tops and ~ 0 ms$^{-1}$ at the surface, $r \sim 2$ and $h$ = 5 km. This rough estimation of the vertical shear agrees with that obtained from the MCD-LMD model for the conditions of storm S1A on 29 May 2019. The model predicted velocities are ~24 ms$^{-1}$ at 5 km altitude and ~ 12 ms$^{-1}$ at the surface giving $\partial u/\partial z \sim$ 2.5 ms$^{-1}$/km.

### 7.5. Rayleigh-Bénard convection similarity

The quasi-regularly spaced cellular structure observed in the textured dust storms resembles the patterns found in classical laboratory experiments of Rayleigh-Bénard convection (RB) and in the cloud patterns in Earth's atmospheric boundary layer (Houze, 2014; Markowski and Richardson, 2011). In Earth two kind of cell patterns are observed: open cellular convection (walls of clouds surrounding open, cloudless areas with descending motions) and close cells (rings of open areas where the air descends surrounding cloudy areas with upward motions) (Houze, 2014; Markowski and Richardson, 2011). According to our images, the Mars's cellular patterns are of the closed type.

One major difference between laboratory RB and atmospheres is the flatness of the cells. The aspect ratio (horizontal length/vertical extent) is $s/h \sim$ 3–5 in laboratory RB experiments where a fluid at rest is heated from below. However, $s/h \sim$ 10–30 in Earth's atmosphere (Agee and Dowell, 1973; Markowski and Richardson, 2011) and $s/h \sim$ 25–100 in closed cellular patterns reported in the equatorial region of Venus upper cloud layer where the cells have sizes of 250–1000 km (Covey and Schubert, 1981; Baker and Schubert, 1992). The aspect ratios for the cellular patterns we have observed on Mars have an ample range of values since for separations between cells $s$ = 20–56-180 km and $h$ = 5 km we get $s/h$ = 4–36, whereas for $h$ = 15 km (from the one-dimensional convection model) we get $s/h$ = 1.3–12. The differences in the aspect ratio between laboratory experiments and atmospheres could be due to intrinsic differences in the conditions organizing convection such as the radiative cooling at cloud tops and the eddy processes and instabilities related to vertical wind shears, both modifying the transport of heat and momentum in the atmospheres.

The cloud streets (HCR) shown in Fig. 7d, e are another example of boundary layer convection. Heavens (2017) denoted the most elongated cases of the periodic linear variations in dust opacity as ruffled textured, and proposed their origin to be analogous to the HCR on Earth. Probably, this is the case for the features shown in Fig. 7. On Earth, the perturbations in temperature, humidity and wind form these coherent patterns (Markowski and Richardson, 2011). The aspect ratios of HCRs in Earth are $s/h \sim$ 3–10 depending on what kind of instability (thermal or wind shear) dominates (Weckwerth et al., 1997, 1999). It is not the purpose of this paper to work further on this part of the observations. We only bring these examples to attention to show that global organized convective patterns are present on Mars in this region and epoch. We

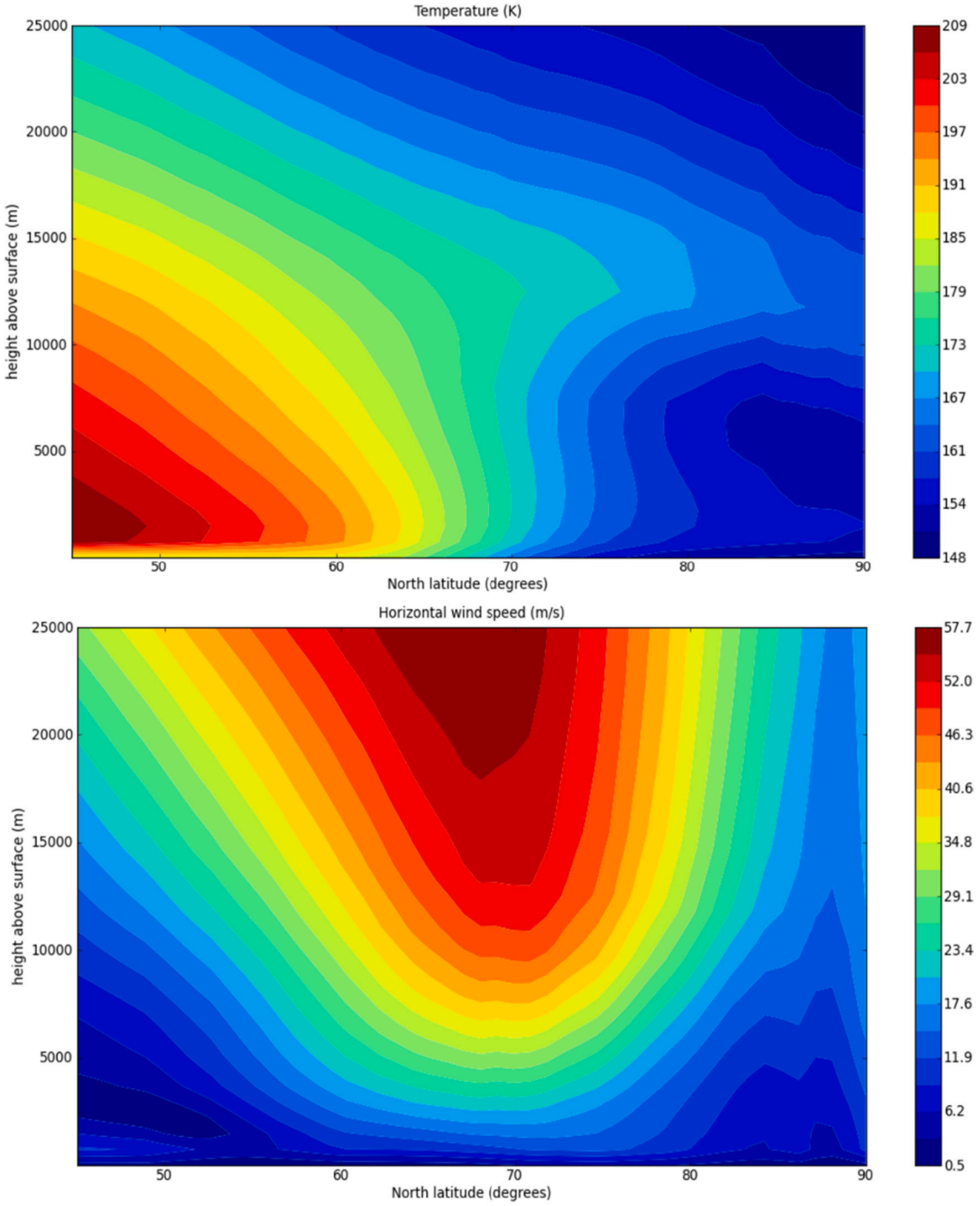


**Fig. 15.** Vertical and meridional distribution of temperature and horizontal wind velocity for 28 May 2019 at 11:01:48 UT (Ls = 31.3°) at longitude 200°E according to the Mars Climate Database (MCD-LMD), corresponding to conditions for the spiral system S1A (Fig. 8).

**Table 4**
Model parameter values.

| Parameter | Range of values |
|---|---|
| $C_D$ | 0.1–2.0 |
| $r_0$ | 100–2500 m |
| $\Delta T_0$ | 0.5–10 K |
| $w_0$ | 0.0002–0.001 $ms^{-1}$ |
| $\ell_C$ | $10^{-6}$–$10^{-3}$ |
| $\alpha$ | 0.2–0.4 |

hope to encourage future research on this topic to provide a comparison with similar phenomena observed on Earth.

## 8. Conclusions

We have presented in this paper a study based on images obtained with three cameras on two space missions, of the dust storms that develop at the northern polar cap boundary of Mars during spring from March to July 2019 (Ls = 350° in MY 34 to 54° in MY 35). We have focused on two storms evolving at Ls = 28°-35° that present a granular texture in large-scale organized patterns. Our main conclusions are:

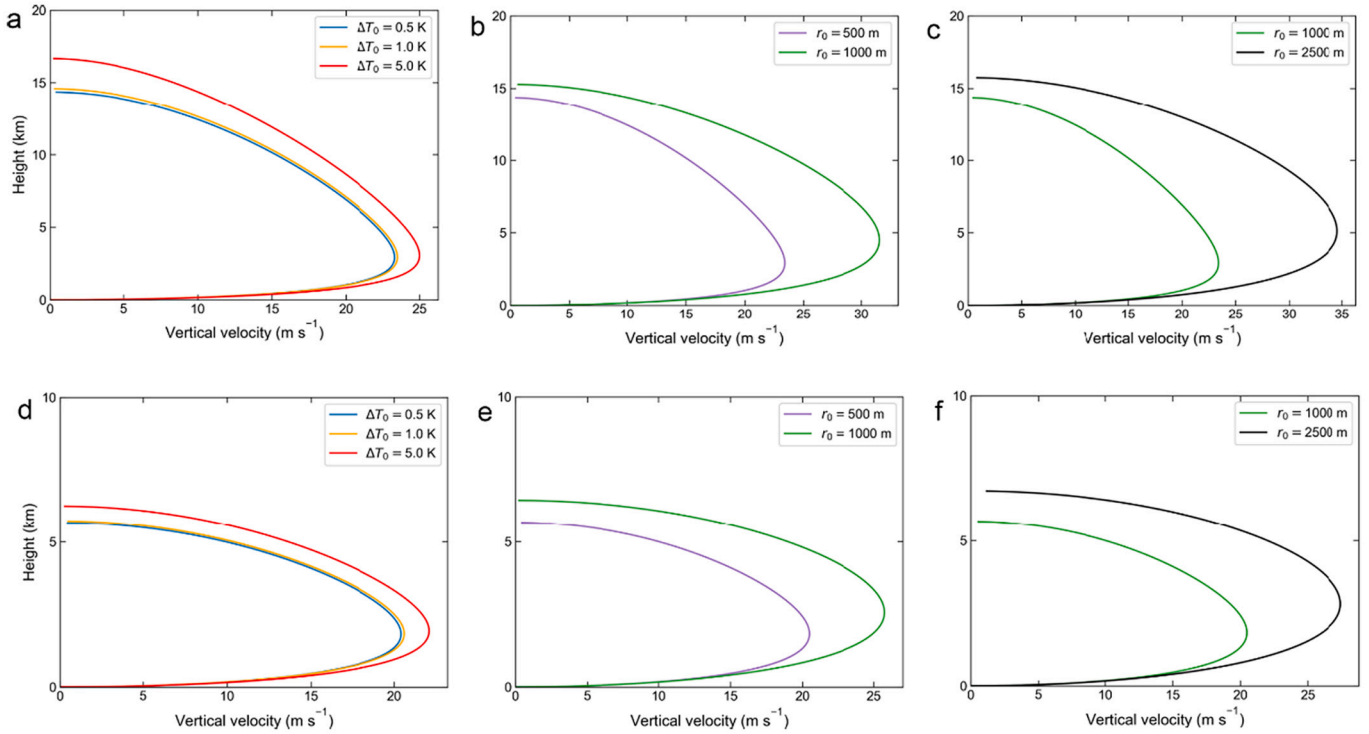


**Fig. 16.** Vertical profile of the velocity of an ascending parcel under different conditions as indicated in the insets. All simulations for $\alpha = 0.2$ and $\ell_C = 10^{-5}$. $\varepsilon = 1$ indicates an adiabatic temperature gradient (a) $\varepsilon = 1$, $C_D = 0.1$, $r_0 = 100$ m; (b) $\varepsilon = 1$, $C_D = 0.5$, $\Delta T_0 = 0.5$ K; (c) $\varepsilon = 1$, $C_D = 1.0$, $\Delta T_0 = 0.5$ K; (d) $\varepsilon = 2$, $C_D = 0.1$, $r_0 = 100$ m; (e) $\varepsilon = 2$, $C_D = 0.5$, $\Delta T_0 = 0.5$ K; (f) $\varepsilon = 2$, $C_D = 1.0$, $\Delta T_0 = 0.5$ K.

- Textured local dust storms are organized in clusters of close anisotropic cells formed typically by 50–100 elements
- These storms form and change or disrupt in hours on a daily basis with a lifetime of ~7–10 days
- They grow in the longitude sector 150°E-210°E centered at latitude ~60°N
- Globally they are shaped as spiral cyclonic vortices or compact dust storms
- The dust mixes with hazes of water ice particles above the polar cap
- Cells in textured areas have typical lengths ~5–10 km, widths ~4–8 km, and separations 30–50 km
- Dust in the cells reaches top altitudes of ~6–11 km above surroundings
- Cells show long tails with lengths ~30–50 km oriented in wind direction
- Groups of cells organize in spatially periodic patterns
- Prevailing winds blow the storms to the east and southeast with speeds 15–45 ms$^{-1}$
- Simultaneously to textured dust storms, "flushing" storms, dust arcs and long and narrow dust filaments form in the longitude sector 300°E-340°E, not showing textured cell patterns.

We propose the following dynamical mechanism to be involved in the formation of textured dust storms:

- The spirals grow as baroclinic instabilities in the intense, vertically sheared eastward jet, generated by the intense meridional temperature gradient
- Local conditions favor this kind of storms in a particular longitude sector
- The frontal systems trigger the rising of the dust by the high speed winds and the intense surface wind stresses
- The cells form by vertical updrafts due to dry convection driven by dust heating, becoming elongated due to vertical wind shears
- Long tails form behind the cells due to windblown dust
- Wave phenomena are involved in the spatial distribution of cells and tails

Future work will focus on the one hand in the search for textured dust storms in other places and epochs on Mars and the comparison of their properties with those reported in this paper. On the other hand, we intend to study the mechanisms that organize dry convection in the cellular patterns and compare them with those acting in similar formations in the terrestrial clouds at the PBL.

## Declaration of Competing Interest

None.

## Acknowledgements

This work has been supported by the Spanish project PID2019-109467GB-I00 (MINECO/FEDER, UE) and Grupos Gobierno *V*asco IT-1742-22. JHB was supported by ESA Contract No. 4000118461/16/ES/JD, Scientific Support for Mars Express Visual Monitoring Camera. The Aula EspaZio Gela is supported by a grant from the Diputación Foral de Bizkaia (BFA). We acknowledge support from the Faculty of the European Space Astronomy Center (ESAC). Special thanks are due to the Mars Express Science Ground Segment and Flight Control Team at ESAC and ESOC.

## References

Agee, E.M., Dowell, K.E., 1973. A review of mesoscale cellular convection. Bull. Am. Meteorol. Soc. 54, 1004–1012.

ArcGis software, 2022. https://www.arcgis.com/index.html.

Baker, Schubert, G., 1992. Cellular convection in the atmosphere of Venus. Nature 355, 710–712.

Barnes, J.R., Pollack, J.B., Haberle, R.M., Leovy, C.B., Zurek, R.W., Lee, H., Schaeffer, J., 1993. Mars atmospheric dynamics as simulated by the NASA Ames general

circulation model 2. Transient baroclinic eddies. J. Geophys. Res. Planets 98 (E2), 3125–3148. https://doi.org/10.1029/92JE02935.
Bell III, J.F., Wol, M.J., Malin, M.C., Calvin, W.M., Cantor, B.A., Caplinger, M.A., Clancy, R.T., Edgett, K.S., Edwards, L.J., Fahle, J., Ghaemi, F., Haberle, R.M., Hale, A., James, P.B., Lee, S.W., McConnochie, T., Noe Dobrea, E., Ravine, M.A., Schaeer, D., Supulver, K.D., Thomas, P.C., 2009. Mars Reconnaissance Orbiter Mars Color Imager (MARCI): instrument description, calibration, and performance. J. Geophys. Res. Planets 114 (E003315), 1–41. https://doi.org/10.1029/2008JE003315.
Cantor, B.A., James, P.B., Caplinger, M., Wolff, M.J., 2001. Martian dust storms: 1999 Mars Orbiter Camera observations. J. Geophys. Res. Planets 106 (E10), 23653–23687. https://doi.org/10.1029/2000JE001310.
Cantor, B., James, P., Calvin, W., 2010. Marci and MOC observations of the atmosphere and surface cap in the north polar region of mars. Icarus 208, 61–81. https://doi.org/10.1016/j.icarus.2010.01.032.
Clancy, R.T., Montmessin, F., Benson, J., Daerden, F., Colaprete, A., Wolff, M.J., 2017. In: Haberle, R.M., Clancy, R.T., Forget, F., Simth, M.D., Zurek, R.W. (Eds.), Mars Clouds. Chapter 5 of the Atmosphere and Climate of Mars. Cambridge University Press, Cambridge, UK. https://doi.org/10.1017/9781139060172.005.
Covey, C., Schubert, G., 1981. Mesoscale convection in the clouds of Venus. Nature 290, 17–20. https://doi.org/10.1038/290017a0.
del Río-Gaztelurrutia, T., Sánchez-Lavega, A., Hernández-Bernal, J., Angulo, A., Hueso, R., Cardesín-Moinelo, A., Martin, P., Wood, S., Titov, D., 2021. Analysis of the Evolution of Martian Polar Caps during Martian Years 34–35 from Mars Express Visual Monitoring Camera, 23rd EGU General Assembly, 19–30 April, 2021, EGU21–7787. https://doi.org/10.5194/egusphere-egu21-7787.
Forget, F., Hourdin, F., Foumier, R., Hourdin, C., Talagrand, O., Collins, M., Lewis, S.R., Read, P.L., 1999. Improved general circulation models of the Martian atmosphere from the surface to above 80 km. J. Geophys. Res. Planets 104, 24155–24176. https://doi.org/10.1029/1999JE001025.
Guzewich, S.D., Toigo, A.D., Kulowski, L., Wang, H., 2015. Mars orbiter camera climatology of textured dust storms. Icarus 258, 1–13. https://doi.org/10.1016/j.icarus.2015.06.023.
Gwinner, K., Jaumann, R., Hauber, E., Hoffmann, H., Heipke, C., Oberst, J., Neukum, G., Ansan, V., Bostelmann, J., Dumke, A., Elgner, S., Erkeling, G., Fueten, F., Hiesinger, H., Hoekzema, N.M., Kersten, E., Loizeau, D., Matz, K.D., McGuire, P.C., Mertens, V., Michael, G., Pasewaldt, A., Pinet, P., Preusker, F., Reiss, D., Roatsch, T., Schmidt, R., Scholten, F., Spiegel, M., Stesky, R., Tirsch, D., van Gasselt, S., Walter, S., Wählisch, M., Willner, K., 2016. The high-resolution stereo camera (HRSC) of Mars express and its approach to science analysis and mapping for Mars and its satellites. Planet. Space Sci. 126, 93–138. https://doi.org/10.1016/j.pss.2016.02.014.
Heavens, N.G., 2017. Textured dust storm activity in Northeast Amazonis–Southwest Arcadia, Mars: phenomenology and dynamical interpretation. J. Atmos. Sci. 74, 1011–1037. https://doi.org/10.1175/JAS-D-16-0211.1.
Heavens, N.G., Richardson, M.I., Kleinböhl, A., Kass, D.M., McCleese, D.J., Abdou, W., Benson, J.L., Schofield, J.T., Shirley, J.H., Wolkenberg, P.M., 2011. Vertical distribution of dust in the Martian atmosphere during northern spring and summer: high-altitude tropical dust maximum at northern summer solstice, 2010. J. Geophys. Res. Planets 116, 1–16. https://doi.org/10.1029/2010JE003692. E01007.
Heavens, N.G., Kass, D.M., Shirley, J.H., Piqueux, S., Cantor, B.A., 2019. An observational overview of dusty deep convection in Martian dust storms. J. Atmos. Sci. 76, 3299–3326. https://doi.org/10.1175/JAS-D-19-0042.1.
Hernández-Bernal, J., Sánchez-Lavega, A., del Río-Gaztelurrutia, T., Hueso, R., Cardesín-Moinelo, A., Ravanis, E.M., Tivov, D., Wood, S., 2019. The 2018 Martian global dust storm over the south polar region studied with MEx/VMC. Geophys. Res. Lett. 46, 10330–10337. https://doi.org/10.1029/2019GL084266.
Hernández-Bernal, J., Sánchez-Lavega, A., Río-Gaztelurrutia, T.D., Ravanis, E., Cardesín-Moinelo, A., Connour, K., et al., 2021. E. an extremely elongated cloud over Arsia Mons volcano on Mars: I. Life cycle. J. Geophys. Res. Planets 126. https://doi.org/10.1029/2020JE006517 e2020JE006517.
Hinson, D.J., 2006. Radio occultation measurements of transient eddies in the northern hemisphere of Mars. J. Geophys. Res. 111, E05002. https://doi.org/10.1029/2005JE002612.
Hinson, D.J., Wilson, J.R., 2021. Baroclinic waves in the northern hemisphere of Mars as observed by the MRO Mars climate sounder and the MGS thermal emission spectrometer. Icarus 357, 114152. https://doi.org/10.1016/j.icarus.2020.114152.
Holton, J.R., 2004. An Introduction to Dynamic Meteorology, 4th edition. Elsevier.
Houze, R.A., 2014. Chap.5 & 6. In: Cloud Dynamics, International Geophysics Series, , 2nd ed.Vol. 53. Academic Press, San Diego, USA.
Hunt, G.E., James, P.B., 1979. Martian extratropical cyclones. Nature 278, 531–532. https://doi.org/10.1038/278531a0.
ISIS, 2022. Integrated Software for Imagers and Spectrometers. https://isis.astrogeology.usgs.gov/ (accessed 2022).
James, P.B., Hollingsworth, J.L., Wol, M.J., Lee, S.W., 1999. North polar dust storms in early spring on Mars. Icarus 138, 64–73. https://doi.org/10.1006/icar.1998.6060.
Jaumann, R., Neukum, G., Behnke, T., Duxbury, T.C., Eichentopf, K., Flohrer, J., Gasselt, S.V., Giese, B., Gwinner, K., Hauber, E., Hoffmann, H., Hoffmeister, A., Köhler, U., Matz, K.-D., McCord, T.B., Mertens, V., Oberst, J., Pischel, R., Reiss, D., Ress, E., Roatsch, T., Saiger, P., Scholten, F., Schwarz, G., Stephan, K., Wählisch, M., 2007. The high-resolution stereo camera (HRSC) experiment on Mars express: instrument aspects and experiment conduct from interplanetary cruise through the nominal mission. Planet. Space Sci. 55, 928–952. https://doi.org/10.1016/j.pss.2006.12.003.
Khare, M.A., Murphy, J.R., Newman, C.E., Wilson, R.J., Cantor, B.A., Lemmon, M.T., Wolff, M.J., 2017. In: Haberle, R.M., Clancy, R.T., Forget, F., Simth, M.D., Zurek, R.W. (Eds.), The Mars Dust Cycle, Chapter 10 of the Atmosphere and Climate of Mars. Cambridge University Press, Cambridge, UK. https://doi.org/10.1017/9781139060172.010.
Kulowski, L., Wang, H., Toigo, A.D., 2017. The seasonal and spatial distribution of textured dust storms observed by Mars Global Surveyor Mars Orbiter Camera. Adv. Space Res. 59, 715–721. https://doi.org/10.1016/j.asr.2016.10.028.
Kundu, P.K., Cohen, I.M., 2008. Fluid Mechanics, 4th ed. Elsevier.
Lin, Yuh-Lang, 2007. Mesoscale Dynamics. Cambridge University Press, pp. 266–267.
Malin, M.C., Calvin, W.M., Cantor, B.A., Clancy, R.T., Haberle, R.M., James, P.B., Thomas, P.C., Wolff, M.J., Bel, J.F., Lee, S.W., 2008. Climate, weather, and north polar observations from the Mars reconnaissance orbiter Mars color imager. Icarus 194, 501–512. https://doi.org/10.1016/j.icarus.2007.10.016.
Markowski, P., Richardson, Y., 2011. Mesoscale Meteorology in Midlatitudes. Wiley-Blackwell.
Millour, E., et al., 2018. The Mars Climate Database (Version 5.3). Scientific Workshop: "From Mars Express to ExoMars".
Newman, C.E., Lewis, S.R., Read, P.L., Forget, F., 2002. Modeling the Martian dust cycle 2. Multiannual radiatively active dust transport simulations. J. Geophys. Res. Planets 107 (E12), 1–15. https://doi.org/10.1029/2002JE001920, 5124.
Odaka, M., 2001. A numerical simulation of martian atmospheric convection with a two-dimensional anelastic model: a case of dust-free Mars. Geophys. Res. Lett. 25, 895–898. https://doi.org/10.1029/2000GL012090.
Odaka, M., Nakajima, K., Takehiro, S.-I., Ishiwatari, M., Hayashi, Y.-Y., 1998. A numerical study of the Martian atmospheric convection with a two-dimensional anelastic model. Earth Planets and Space 50 (5), 431–437. https://doi.org/10.1186/BF03352130.
Ordoñez-Etxeberria, I., Hueso, R., Sanchez-Lavega, A., Vicente-Retortillo, A., 2020. Characterization of a local dust storm on Mars with REMS/MSL measurements and MARCI/MRO images. Icarus 338 (113521), 1–19. https://doi.org/10.1016/j.icarus.2019.113521.
QGIS, 2022. A Free and Open Source Geographic Information System. https://qgis.org/en/site/ (accessed 2022).
Read, P.L., Lewis, S.R., Mulholland, D.P., 2015. The physics of Martian weather and climate: a review. Rep. Prog. Phys. 78 (125901), 1–54. https://doi.org/10.1088/0034-4885/78/12/125901.
Sánchez-Lavega, A., 2011. An Introduction to Planetary Atmospheres. Taylor-Francis-CRC, Florida (USA).
Sánchez-Lavega, A., Chen-Chen, H., Ordoñez-Etxeberria, I., Hueso, R., del Río-Gaztelurrutia, T., Garro, A., Cardesín-Moinelo, A., Titov, D., Wood, S., 2018a. Limb clouds and dust on Mars from images obtained by the Visual Monitoring Camera (VMC) onboard Mars express. Icarus 299, 194–205. https://doi.org/10.1016/j.icarus.2017.07.026.
Sánchez-Lavega, A., Garro, A., del Río-Gaztelurrutia, T., Hueso, R., Ordoñez-Etxeberria, I., Chen Chen, H., Cardesín-Moinelo, A., Titov, D., Wood, S., Almeida, M., Spiga, A., Forget, F., Määttänen, A., Hoffmann, H., Gondet, B., 2018b. A seasonally recurrent annular cyclone in Mars northern latitudes and observations of a companion vortex. J. Geophys. Res. Planets 123, 3020–3034. https://doi.org/10.1029/2018JE005740.
Sánchez-Lavega, A., del Río-Gaztelurrutia, T., Hernández-Bernal, J., Delcroix, M., 2019. The onset and growth of the 2018 Martian global dust storm. Geophys. Res. Lett. 46, 6101–6108. https://doi.org/10.1029/2019GL083207.
Simpson, J., 1971. On cumulus entrainment and onedimensional models. J. Atmos. Sci. 28, 449–455. https://doi.org/10.1175/1520-0469(1971)028<0449:OCEAOD>2.0.CO;2.
Spiga, A., Faure, J., Madeleine, J.B., Määttänen, A., Forget, F., 2013. Rocket dust storms and detached dust layers in the Martian atmosphere. J. Geophys. Res. Planets 118, 746–767. https://doi.org/10.1002/jgre.20046.
Stommel, H., 1947. Entrainment of air into a cumulus cloud. J. Meteorol. 4, 91–94. https://doi.org/10.1175/1520-0469(1947)004<0091:EOAIAC>2.0.CO;2.
Tyler Jr., D., Barnes, J.R., 2005. A mesoscale model study of summertime atmospheric circulations in the north polar region of Mars. J. Geophys. Res. Planets 110 (E06007), 1–26. https://doi.org/10.1029/2004JE002356.
Vallis, G.K., 2006. Atmospheric and Ocean Fluid Dynamics, Fundamentals and Large-Scale Circulation. Cambridge University Press.
Wang, H., Fisher, J.A., 2009. North polar frontal clouds and dust storms on Mars during spring and summer. Icarus 204, 103–113. https://doi.org/10.1016/j.icarus.2009.05.028.
Wang, H., Ingersoll, A.P., 2002. Martian clouds observed by Mars global surveyor Mars orbiter camera. J. Geophys. Res. Planets 107 (E10), 1–16. https://doi.org/10.1029/2001JE001815, 5078.
Wang, H., Zurek, R.W., Richardson, M.I., 2005. Relationship between frontal dust storms and transient eddy activity in the northern hemisphere of Mars as observed by Mars Global Surveyor. J. Geophys. Res. 110, E07005 https://doi.org/10.1029/2005JE002423.
Weckwerth, T.M., Horst, T.W., Wilson, J.W., 1999. An observational study of the evolution of horizontal convective rolls. Mon. Weather Rev. 127, 2160–2179.
Weckwerth, T.M., Wilson, J.W., Wakimoto, R.M., Andrew-Crook, N., 1997. Horizontal convective rolls: determining the environmental conditions supporting their existence and characteristics. Mon. Weather Rev. 125, 505–526. https://doi.org/10.1175/1520-0493(1997)125<0505:HCRDTE>2.0.CO;2.